Master of Science Thesis

Chemical mitigation options for gas reservoir compaction: a preliminary assessment in the context of seismic and subsidence hazard analysis

Mariska Schimmel

February 2015

Supervisors:

Prof. Dr. C.J. Spiers

Dr. S.J.T. Hangx

Dr. Ir. C.A. Ramirez

Universiteit Utrecht

Abstract

Natural gas, being a cleaner fossil fuel, is part of both European and national strategies to reduce CO_2 emissions and to facilitate the switch to a more sustainable energy system. However, the penetration of natural gas into the energy system is threatened by unwanted effects of gas production: reservoir compaction, surface subsidence and induced seismicity. Compaction creep of the gas reservoir is not well understood, neither is the mitigation of creep. Consequently, model predictions for gas reservoirs concerning the volume of gas in place, the seismic hazard, or the amount of surface subsidence, are prone to error.

In this study, two types of uniaxial compaction experiments are conducted on quartz sand aggregates to improve the understanding of compaction creep and to investigate possible mitigation measures. To this extent, grain size and compaction stress remained constant, while various pore fluids were tested. Besides lab air, this included silica saturated, acid, alkaline, aluminium and AMP solutions. In addition, three different analyses (one deterministic by TNO and two probabilistic by the KNMI and NAM) of seismic hazard of Dutch gas fields are examined in a literature review, in order to identify how reservoir compaction is incorporated.

From the experiments, it is inferred that initial time-independent deformation is mainly controlled by grain rearrangement and microcracking. Subsequent time-dependent deformation (i.e. compaction creep) is controlled by subcritical crack growth, which is enhanced by the presence of water (i.e. stress corrosion cracking). Furthermore, it is found that AMP has an inhibiting effect on compaction creep, because it prevents the wetting of the crack-tip. From the literature review, it appeared that each analysis incorporates reservoir compaction differently. In the deterministic approach by TNO, reservoir compaction was indirectly incorporated via an elastic parameter. In the probabilistic study the KNMI, there was very limited integration of reservoir compaction: either there is compaction and seismicity, or there is no compaction and no seismicity. In the probabilistic analysis by the NAM, reservoir compaction was thoroughly integrated. To model surface subsidence, the NAM developed different compaction models (bi-linear and time-decay). Interestingly, the models predicted similar subsidence trends.

Table of Content

1 Introduction

Natural gas plays an important role in the European energy system. In 2011, natural gas accounted for 18 % of European primary energy production, while for the Netherlands it represented almost 90 % [1]. By 2035, global energy demand is expected to increase by one-third compared to 2011 [2], and consequently the demand for natural gas will increase. Natural gas, being a cleaner fossil fuel, is part of both European and national strategies to reduce CO_2 emissions and to facilitate the switch to a more sustainable energy system [2–5]. However, decades of gas production have resulted in reservoir compaction, surface subsidence and induced seismicity [6]. In recent years, these effects have been increasingly observed in many countries, notably in the giant Groningen gas field (the Netherlands) [7,8]. These unwanted effects have significant impact on the environment, surface infrastructure and public opinion [9], which can potentially influence the penetration of natural gas into the energy system. In the Netherlands, these effects also impact the national economy and increase national dependency on gas imports.

During the producing life-time of a gas reservoir, the reservoir pressure decreases. This activates poroelastic compaction of the rock as well as permanent compaction by time-dependent creep [6,8,10,11]. Compaction creep is controlled by chemical-mechanical processes, which are not well understood. It is known that the injection of high-pressure fluids (like, air, CO_2 and nitrogen) in producing gas reservoirs can stabilize reservoir pressure and mitigate the poroelastic compaction of the sandstone reservoir [8]. Injection of fluids for pressure maintenance reduces the mechanical driving force for compaction creep. However, there may also be additional chemical effects influencing creep. For example, some chemical additives are known to enhance (Na^+ [12,13]) or inhibit (Al^{3+} [13]) creep in sands and sandstones. Furthermore, compaction creep in sand(stone) is enhanced by alkaline fluids and inhibited by acidic fluids (e.g. CO_2) [10,11,13]. Nonetheless, compaction creep is a complex chemical-mechanical process that depends on many factors, like pore fluid composition and pH, grain size, temperature and effective stress [12,14,15]. As a consequence, compaction creep is still poorly understood and poorly described, with predictive microphysical models lacking. In addition, chemical effects of other additives (e.g. phosphonates and surfactants) on creep in sand(stone)s, and the possibility of mitigating reservoir compaction by pore fluid manipulation, have not been investigated systematically.

As a result of the poor understanding of compaction creep, compaction of the gas reservoir is not well constrained. The poroelastic compaction of the reservoir is studied extensively, e.g., [16–19], but the effect of creep on reservoir compaction is rarely considered [20]. Consequently, model predictions for reservoirs concerning the volume of gas present, the seismic hazard or the amount of surface subsidence, may be prone to large errors. In the Netherlands, these predictions are essential components of the production plans for gas fields [21]. Over- or underestimating these components can have a significant impact on licensing, expected revenue and public opinion.

The aim of this study is twofold. Firstly, it aims to get a preliminary understanding of potential agents that can mitigate compaction creep in gas fields in the Netherlands. Secondly, the study aims to get a preliminary understanding of the incorporation of reservoir compaction in models that predict the seismic hazard or surface subsidence related to gas fields in the Netherlands.

These two aims are unified in the ambition to have a better the link between the results from small-scale experimental work and the large-scale system the results contribute to.

Concerning the first aim, the study investigates the mechanisms controlling compaction creep and the influence of various types of fluids on it. To this extent, experiments are performed using two types of uniaxial compaction set-ups. The first compaction set-up is characterized by its simplicity and has the advantage that simultaneously multiple experiments can be performed. The second compaction set-up is located in an Instron loading frame and produces well controlled experiments. Experiments in both set-ups were performed with quartz sand as sample material. While grain size and compaction stress remained constant, the type of pore fluids was varied. This includes pore fluids for baseline experiments (lab air and silica saturated solution) and multiple other solutions, like acid, alkaline, aluminium and AMP.

In order to fulfil the second aim, a literature review into hazard analysis is performed. The focus is on methods used to analyse the seismic hazard of gas fields in the Netherlands. Two types of methods are examined: deterministic and probabilistic. The deterministic seismic hazard analysis was conducted by the research institute TNO (Nederlandse Organisatie voor Toegepast Natuurwetenschappelijk Onderzoek), while a more complex probabilistic seismic hazard analysis was performed by both the KNMI (Koninklijk Nederlands Meteorologisch Instituut) and the NAM (Nederlandse Aardolie Maatschappij). In addition, the NAM developed compaction model to also model surface subsidence.

In this report, first the experimental work is presented, which is followed by the literature review on seismic hazard analyses. Chapters 2 reports the methodology and findings from the simple set-up experiments. Chapter 2 is subdivided in three sections, because three different testing procedures were tried. Each section explains one of these testing procedures, presents the associated results and discusses the effectiveness of the selected testing procedure. A similar structure is used in Chapter 3, which describes the experiments performed using the Instron loading frame. Based on this set-up, two different testing procedure were tried, which are explained in two different sections, each containing a methodology, results and discussion. Chapter 4 briefly introduces the parameters involved in calculating the compaction of a reservoir, in order to provide some necessary background knowledge for Chapter 5 and 6. Chapter 5 reports the literature review of seismic hazard analyses. It starts with a description of deterministic seismic hazard analysis and a review of the TNO study. This is followed by a description of probabilistic hazard analysis and a review of the KNMI and the NAM study. Each review is followed by a small discussion about the incorporation of reservoir compaction in the analysis. In Chapter 6, the compaction models used by the NAM to predict surface subsidence are described and the predicted subsidence due to reservoir compaction is presented.

2 Steel Tube Experiments

Steel tube experiments refer to experiments performed using a simple uniaxial compaction set-up. This method has been proven to be successful when studying the compaction behaviour of salts [22–24]. However, it had not been tested yet for harder materials, such as quartz. Though simple, the set-up produced unexpected, inconsistent and unreasonable results when tried on quartz. In order to improve the results, the testing procedure was changed multiple times. Three stages are defined for which the testing procedure changed, while the other components of the methodology remained the same. To avoid repetition, first the general methodology is explained. This includes a description of the sample preparation, pore fluid preparation, experimental set-up, and data acquisitioning and processing. Next, for each stage the testing procedure is explained, followed by a presentation of the results and a discussion about the testing procedure and the obtained data.

2.1 Sample Preparation and General Methods

2.1.1 Sample Preparation

The sample material used in the steel tube experiments comes from a large batch of quartz sand of unknown origin. The sand was grinded by hand using a mortar and pestle, and subsequently sieved to a grain size fraction of 90 µm to 125 µm. With this grain size range, the sample contains more than ten adjacent grains in its diameter. This is necessary to minimalize boundary effects, like friction between the grains and tube walls. The selected grain size fraction was washed with distilled water to remove the fines attached to the grain surfaces. Subsequently, the material was left to dry for several days at 50 °C.

2.1.2 Pore Fluid Preparation

The steel tubes experiments were performed using a number of different pore fluids (Tables 1, 2 and 3). Reference experiments were conducted using lab air, distilled water or silica saturated solution as pore fluid. The silica saturated solution was created by dissolving a fixed volume of sodium metasilicate ($Na_2SiO_3 \bullet 9H_2O$) in distilled water. After a thorough stirring, the mixture was diluted to create a solution containing 255 ppm silica. At 25 °C and 0.1 MPa, this is an oversaturated silica solution [25–27].

Other pore fluids investigated were solutions containing acid, base, aluminium, amino methylene phosphate (AMP), washing detergent or mTA. These were prepared by dissolving fixed amounts of certain substances in distilled water and diluting the mixtures. A fixed amount of HCl and NaOH was dissolved to obtain an acid solution (pH 3) and an alkaline solution (pH 11), respectively. $AlCl_3$ was dissolved and diluted to attain the aluminium solution with an Al^{3+} concentration of 0.076 g/L and a pH of 3.5. The AMP solution contained 1 ‰ AMP in percentage of total solution and was created by dissolving a fixed volume of AMP. AMP is an additive used in a vast variety of industries to inhibit scaling and corrosion [28–31]. Next, a fixed amount of washing detergent powder (Robijn Fleur en Fijn) was dissolved, creating a 6 g/L washing detergent solution. This concentration is the advised concentration for washing clothes. The final solution was a 16 % mTA solution, which was provided by AkzoNobel. mTA is a biodegradable chemical developed by AkzoNobel that prevents the caking of salt [32,33].

2.1.3 Experimental Set-Up

The experiments were performed using a small-scale, dead weight, 1-D (uniaxial) compaction set-up (Figure 1) [22–24]. The so-called compaction vessel is a steel tube with a diameter of 1.6

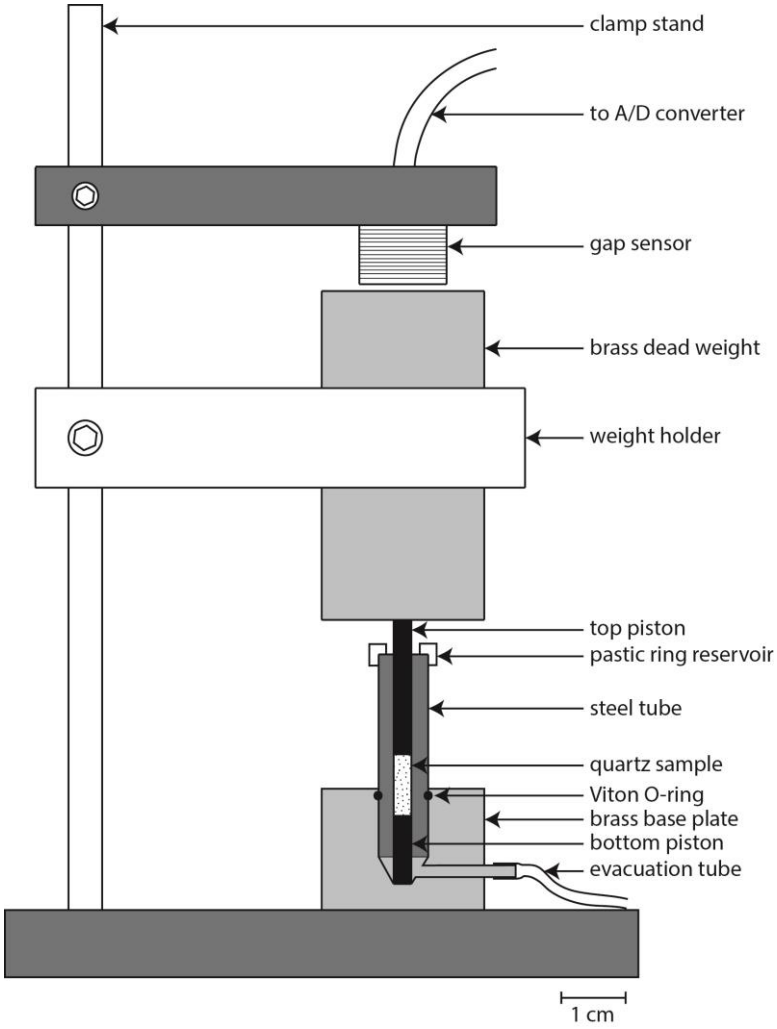

Figure 1: Schematic diagram of the steel tube set-up.

mm, which allows the use of relatively small weights to generate high stresses. The lower end of the steel tube is placed in a brass base plate, forming a stable structure. The presence of a Viton O-ring in the base plate ensures a tight fit and prevents the upward escape of pore fluid. The base plate has an evacuation tube (fluid outlet), which can be used to rapidly flood the sample by applying a partial vacuum. At the upper end of the steel tube, a plastic ring is placed, which acts as a pore fluid reservoir.

The steel top and bottom pistons are close-fitting. With the lower piston and (dummy) sample in place, the top piston protrudes from the steel tube and fluid reservoir; on top a dead-weight can be placed. The displacement of the dead-weight is measured using a gap sensor transducer (Baumer Electric, type IWA 18U 9001, full scale 1.5 mm, output signal 2-8 V). It is assumed that the displacement of the dead-weight fully reflects the displacement of the sample.

In total four of such assemblies exist, which can be used simultaneously. The four set-ups are located in a Styrofoam box in order to have a stable and controlled temperature during the experiment. A fan and lamp connected to a temperature controller maintain the box temperature at 30 °C. A thermocouple placed in the back of the box measures the temperature of the box. It must be noted that during the first half of the Stage I (up to experiment T9) the temperature box was not yet in place. After performing multiple experiments it became

appeared that it was necessary to better control the temperature and the Styrofoam box was installed.

2.1.4 Data Acquisitioning and Processing

Throughout the experiment, the gap sensor voltage signal for the four set-ups and box temperature were logged every 5 seconds using a 16-bit NI DAQPad-6015 A/D converter, which was connected to a PC. Gap voltage was translated to gap distance based on a calibration. This calibration was made by placing a dial gouge on top of the gap sensor, moving the sensor with known distances and recording the associated voltage values. Between 2 V and 8 V this relation is linear, which corresponds to a maximum gap distance of 1.5 mm. To the linear part of the data, a least-square fit was made, which was used to translate the gap voltage to gap distance.

Based on the gap distance sample length, volumetric strain and porosity was calculated as a function of time. The starting point for all the calculation was chosen to be (approximately) the first moment in time where the dead weight touched the sample. In uniaxial experiments, the instantaneous volumetric strain $e_v = -\frac{\Delta V}{V_0}$ equals the instantaneous axial strain $e_v = -\frac{\Delta L}{L_0}$, because the sample can only deform along its length.

2.2 Stage I: Testing Various Liners to Reduce Wall Friction

2.2.1 Testing Procedure

The experiments performed during Stage I have slightly varying testing procedures, because various ideas were tested. As the testing procedure is explained, these differences are pointed out.

In some experiments, the steel tubes were lined with graphite powder, heat shrink tube or Teflon (Table 1) to reduce the friction between the grains and the tube walls. The graphite (from Kremer Pigments) is a very fine powder, which easily sticks to surfaces and provides a smooth layer. When used in experiments, the graphite powder was funnelled into the steel tube after which the steel tube was shaken (with the ends closed) to distribute the powder evenly. Surplus

Table 1: Experimental details of Steel Tube Experiment Stage I

	σ_{pre} [MPa]	t_{pre} [hours]	σ_{comp} [MPa]	t_{comp} [hours]	Pore Fluid	φ_0 [%]	e_v [%]
T1 [a]			3.90	1.2	Lab air	27.9	0.27
T2 [b]			3.90	2.6	Lab air	33.2	
T3 [a]			7.37	2.2	Lab air/Distilled water	29.3	0.47
T4 [b]			7.37	2.6	Distilled water [d]	30.2	0.34
T5 [a]			7.37	2.1	Distilled water [d]	26.9	0.40
T6 [a]	7.37	1.5	6.78	43.8	Distilled water	23.8	0.47
T9 [c]	7.37	0.75	6.78	188.1	Distilled water	30.0	2.60
T10	7.37	1	7.37	21.1	Distilled water	25.5	0.44
T11			7.37	114	Lab air/Distilled water	40.0	0.45
T12.1	11.50	0.33	11.50	354.5	Silica saturated solution [d]	42.3	1.04
T12.2	11.50	0.33	11.50	354.6	Silica saturated solution [d]	48.0	0.29
T12.3	11.50	0.33	11.50	354.6	Lab air	40.6	0.28
T12.4	11.50	0.33	11.50	354.6	Lab air	41.1	1.02
T13.1	11.50	1	11.50	502.9	HCl solution [d]	43.9	1.01
T13.2	11.50	1	11.50	502.9	NaOH solution [d]	41.9	0.26
T14.1			11.50	118.5	Lab air/HCl solution	48.7	1.86
T14.2			11.50	118.6	Lab air/NaOH solution	41.7	2.82

[a] no liner, [b] graphite powder, [c] heat shrink tube, others lined with Teflon. [d] fluid added prior to loading.

powder was removed by tapping the steel tube on the table. The second liner, heat shrink tube, is a material that shrinks when heated. A 8 mm long, closely fitted tube was created by carefully shrinking the heat-shrink tube around the smooth end of a drill bit (diameter 1.5 mm). The third liner, Teflon, was cut from a large sheet of Teflon and subsequently rolled into a cylinder (8 mm long) and slide into the steel tube.

After the steel tube was lined with the appropriate liner, the bottom piston was inserted and the steel tube was placed in the base plate, upon which approximately 18 mg of sample material was carefully funnelled into the steel tube. Next, the top piston was inserted, the pore fluid reservoir added on top and the evacuation tube connected. The assembly was tapped multiple times to allow the grains to rearrange and its length was measured using a calliper. Based on this length, the starting length of the sample is calculated by subtracting the lengths of the various components (e.g. top and bottom piston) from the assembly length.

For the experiments that had a pre-compaction phase (Table 1), the pre-compaction weight was put in place and the gap sensor adjusted to ensure that the gap distance was in measuring range. Next, the sample was placed in the temperature box and box was kept close for several moments to stabilize temperature. Once temperature was stable, the sample was carefully placed under the dead weight and allowed to pre-compaction. The pre-compaction time varied per experiment, ranging from 20 minutes to 1.5 hours (Table 1). The pre-compaction phase was terminated by carefully lifting the dead weight and removing the sample. Again the assembly length was measured.

If necessary, the pre-compaction weight was changed for the compaction weight and accordingly the gap sensor was adjusted. With some experiments, the pore fluid was added to the sample before placing it under weight (Table 1). To do so, the fluid reservoir was filled with the selected pore fluid and by applying a partial vacuum using the evacuation tube, the sample was wetted almost instantaneously. After flooding the sample, the evacuation tube was closed off and a drop of silicon oil was added to the fluid reservoir to prevent evaporation of the pore fluid. Next, the sample was carefully placed under the dead weight. For the experiments that had the pore fluid added while under load (Table 1), this was done a few minutes after placing the sample under the dead-weight and in a similar manner as described above. The experiments were terminated by carefully removing the dead weight. After the assembly length was measured, it was dissembled and the sample was carefully removed from the steel tube and placed in a small cup for dry storage at 50 °C.

2.2.2 Results

In total 17 experiments were performed, a selection is presented in Figures 2-5. Figure 2 illustrates strain versus time curves of one dry experiment (T1) and two wet experiments (T4 and T5). Even though the wet experiments either experienced a decrease in strain at the end of the experiment (T4) or a sudden drop in strain halfway the experiment (T5), both experienced clearly more strain than the dry experiment (T1). In addition, Figure 2 shows a strain curve of an initially dry experiment to which distilled water was added after 45 minutes (T3). Once the fluid is added, the strain curve shows an immediately, but irregular, increase. It must be noted that these experiments were performed without the temperature box. Furthermore, the experiments were performed without a liner to reduce friction, except for T4 which was lined with graphite powder.

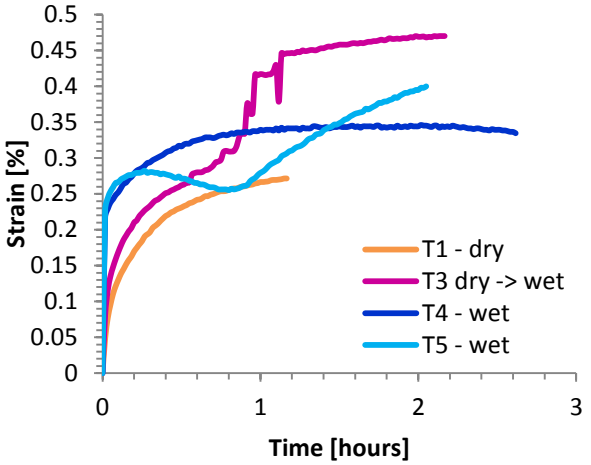

Figure 2: Strain versus time diagram showing the difference between wet and dry compaction creep.

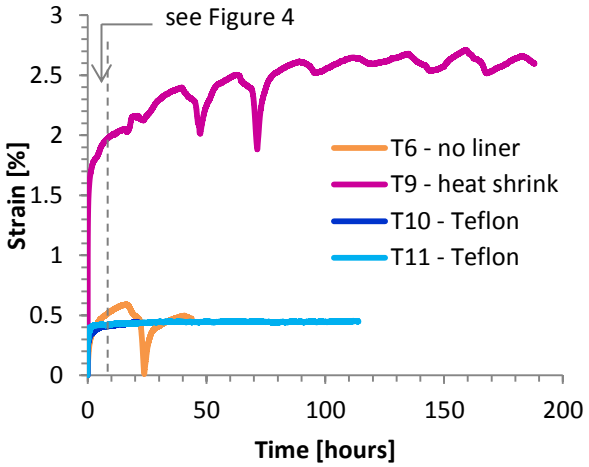

Figure 3: Strain versus time diagram showing the effect of the respective liner on compaction.

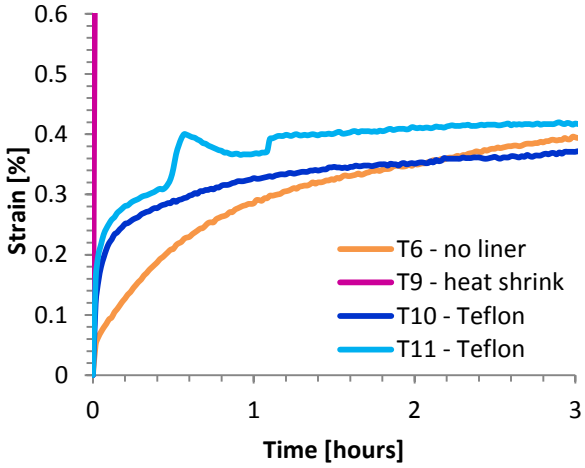

Figure 4: Enlargement of the first three hours of Figure 3 showing the effect of adding the pore fluid while under load (T11).

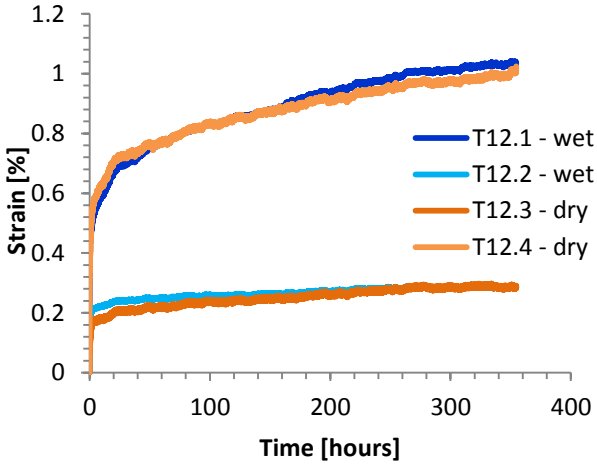

Figure 5: Strain versus time diagram showing the difference between wet and dry compaction creep. The presented experiments are performed simultaneously in the temperature box.

Figure 3 depicts strain versus time curves of four distilled water experiments, which were first pre-compacted. An exception is T11, which was not pre-compacted, but started compaction dry and was wetted after half an hour. Figure 4 is an enlargement of Figure 3 and clearly illustrates this wetting effect. While T10 and T11 have very similar strain curves and T6 is more or less similar, T9 shows more strain. T10 and T11 were both lined with Teflon and T6 had no liner, while T9 was lined with heat shrink tube. Another difference between the experiments is the temperature box, which was not yet in place when T6 and T9 were performed. As can be seen in Figure 3, better temperature control improved the stability of the experiments (compare T6 and T9 to T10 and T11).

The last diagram, Figure 5, presents four simultaneously performed experiments. They were performed with the temperature box in place and experienced identical environmental influences. The experiments also had a similar pre-compaction and were all lined with Teflon, the only element that varied was the pore fluid. However, this is not apparent from Figure 5. The two clusters of lines depicted in the diagram are not a cluster of dry experiments and a cluster of wet experiments. On the contrary, they are mixed groups of one dry and one wet experiment.

This shows the poor reproducibility of the experiments and makes it impossible to draw conclusions about the effect of adding a fluid.

2.2.3 Discussion

The results of the performed experiments are unsuitable to define the effect of various fluids on the compaction behaviour of quartz sands, because the results are irregular and show a bad reproducibility. However, the results can be used to define a new testing procedure. In the following section, it is discussed which elements of the testing procedure worked and which not. This discussion serves as the foundation for testing procedure described in the Stage II.

2.2.3.1 Friction Reduction

Quartz grains have a relatively high hardness and the sharp grain edges can therefore easily bite into the walls of the steel tubes. When this happens, the grain is temporarily stuck, postponing compaction. Stresses build up around the stuck grain and once a certain limit is reached the grain breaks free, releasing the concentrated stresses. This results in a sudden increase in compaction. In the strain curves, this effect is visible by the irregular increases in strain (e.g. Figure 2).

Three liners were tried to reduce friction between the grains and vessel walls: graphite powder, heat-shrink tube and Teflon. The graphite is a very fine grained powder, which sticks easily to surfaces and forms a smooth layer. However, due to being so fine and its stickiness the powder got intermingled with the sample material. Upon retrieval from the experiments, some samples had a dark layer of graphite powder sticking to the bottom. This layer increases the sample length and may influence the compaction behaviour. Therefore, the use of this anti-friction liner is not recommended.

The second liner, the heat-shrink tube, proved to be very delicate to make, for it had to be shrunken around the smooth end of a drill bit by carefully heating it. When tried in an experiment (T9), the tube appears to influence the compaction behaviour of the sample, because T9 had much higher instantaneous strains than the other experiments (Figure 3). Upon closer examination, the heat-shrink tube showed to be very elastic. Most likely, the elastic deformation of the heat-shrink tube had a large contribution to the high instantaneous strain observed in T9. This was enough reason to stop further testing with the heat-shrink tube.

The third liner tried was the Teflon liner. The Teflon liner was cut from a large sheet of Teflon and rolled around the smooth end of a drill bit to get a cylindrical shape. It could then be easily inserted in the steel tube. There is no indication that the presence of the Teflon liner had other influences on compaction behaviour of the sample besides reducing the friction. Therefore, it was decided that a Teflon liner should be used to reduce the friction.

2.2.3.2 Temperature

After performing several experiments that lasted longer than a day, it became clear that temperature had a major influence on the recorded displacement. For example, T9 shows major drops and rises in strain, which are most likely related to temperature changes (Figure 6). After the temperature box was installed, the temperature was very stable and the resulting strain curves were less irregular (e.g. Figure 5).

However, adding a fluid while the experiment is in a temperature box comes with difficulties. Opening the box for more than five minutes has an effect on the recorded displacement. For

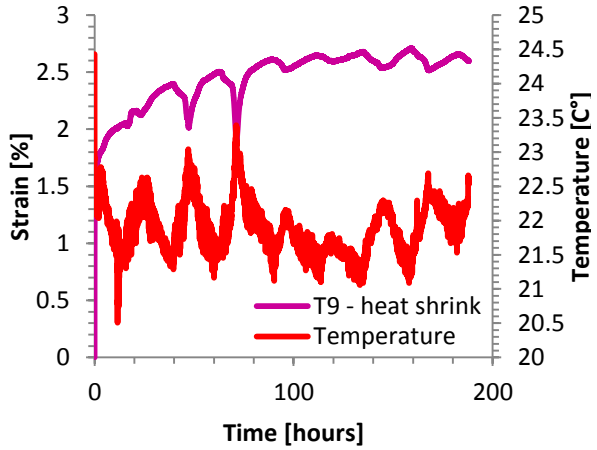

Figure 6: Strain and temperature versus time diagram showing the correlation between temperature changes and strain changes, in the absence of proper temperature control.

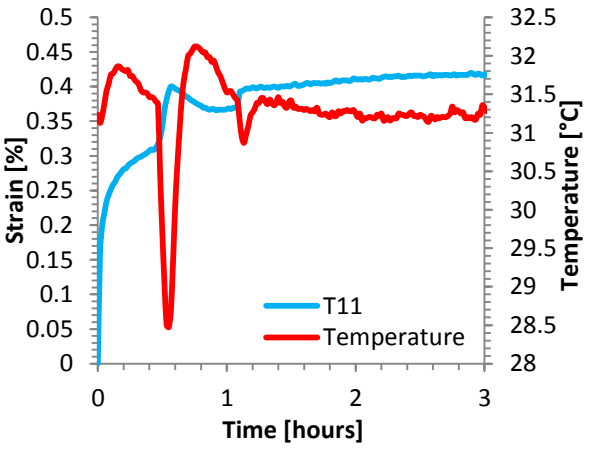

Figure 7: Strain and temperature versus time diagram showing the changes in temperature caused by opening and closing the box to add the pore fluid to the sample.

example, in Figure 7 both strain and temperature are plotted for T11. The opening of the temperature box is characterized by a sudden fall in temperature, while the sudden rise in temperature indicates that the box is closed again. Before temperature is stable again, it overshoots and subsequently lowers again. A reversed pattern is observed in the strain curve. When the temperature drops, the strain increases and vice versa. This relation makes sense, because upon opening the box, the assembly cools down and contracts, increasing the gap between the weight and the gap sensor. When the box is closed again, the assembly heats up and expands, closing the gap between the weight and the gap sensor. This makes it difficult to discern the effect of adding the fluid, which also leads to an increase in strain. The observed increase in strain could be the result of the drop in temperature or the combined result of the temperature change and adding the fluid.

Though the temperature is very unstable for approximately half an hour, overall the temperature box improves the quality of the experiments. During the course of the experiment, a very stable temperature (31.3 ± 0.3 °C for T11 after two hours) is obtained, which results in less irregular strain curves. Therefore, it was decided to continue to perform experiments in the temperature box.

2.3 Stage II: Testing the Effect of Pore Fluid

2.3.1 Testing Procedure

The testing procedure of Stage II is similar to the one described in Stage I. However, instead of varying the friction reducing liner, compaction time and moment of adding fluid, this is all held constant and only the type of pore fluid is varied (Table 2). In Stage II, all the experiments started with an hour of dry pre-compaction using a dead weight of 2355 g (equals a stress of 11.5 MPa). The aim of this is to obtain a constant starting porosity and a locked starting aggregate. After pre-compaction followed three days of wet compaction using a dead weight of 1425 g (equals a stress of 6.95 MPa).

The experiments were performed using approximately 18 mg of sample material. After inserting the Teflon liner and bottom piston into the steel tube, the sample material was carefully funnelled in. Next, the top piston was inserted and the steel tube was placed in the base plate.

The assembly was completed by placing the fluid reservoir and top and connected the evacuation tube. After tapping the assembly multiple times to rearrange the grains, the assembly length was measured using a calliper. This was used to calculate the starting length of sample.

Subsequently, the pre-compaction weight was placed in the set-up and the gap sensor was adjusted so the gap would be in the measuring range. The assembly was placed in the temperature box, after which the box was closed for several moments to stabilize temperature. With the temperature stable, the sample was carefully placed under the weight and left to pre-compact. Pre-compaction was terminated by carefully lifting the dead weight and retrieving the sample. The assembly length was measured again using a calliper.

Next, the compaction weight was placed in the set up and the gap sensor was adjusted accordingly. The temperature box remain again closed for several moments to regain a stable temperature. Once this was obtained, the sample was carefully placed under the dead weight. After approximately five minutes, the pore fluid was added to the fluid reservoir. Using the evacuation tube, a partial vacuum was created which allowed the sample to be quickly flooded. After wetting the sample, the evacuation tube was closed off and a drop of silicon oil was added to the top reservoir to prevent evaporation of the pore fluid. The experiments were terminated

Table 2: Experimental details of Steel Tube Experiment Stage II

	σ_{pre} [MPa]	t_{pre} [hours]	σ_{comp} [MPa]	t_{comp} [hours]	Pore Fluid	φ_0 [%]	e_v [%]
ELA1	11.50	1	6.95	64.5	Lab air	43.6	0.41
ELA2	11.50	1	6.95	64.5	Lab air	38.8	0.23
ESSS1	11.50	1	6.95	64.3	Silica saturated solution	38.8	0.43
ESSS2	11.50	1	6.95	64.5	Silica saturated solution	41.9	0.23
ESSS3	11.50	1	6.95	67.9	Silica saturated solution	44.2	0.33
ESSS4	11.50	1	6.95	67.9	Silica saturated solution	42.4	0.35
ESSS5	11.50	1	6.95	67.9	Silica saturated solution	42.6	0.74
ESSS6	11.50	1	6.95	67.9	Silica saturated solution	42.6	0.60
EACS1	11.50	1	6.95	64.7	HCl solution	42.6	0.51
EACS2	11.50	1	6.95	64.7	HCl solution	40.4	0.63
EACS3	11.50	1	6.95	67.7	HCl solution	41.1	0.52
EACS4	11.50	1	6.95	67.7	HCl solution	46.8	0.51
EALS1	11.50	1	6.95	64.7	NaOH solution	41.7	0.42
EALS2	11.50	1	6.95	64.7	NaOH solution	43.5	0.26
EALS3	11.50	1	6.95	69.3	NaOH solution	41.4	0.58
EALS4	11.50	1	6.95	69.2	NaOH solution	40.0	0.35
EALUS1	11.50	1	6.95	67.7	Aluminium solution	44.2	0.42
EALUS2	11.50	1	6.95	67.7	Aluminium solution	40.6	0.50
EWDS1	11.50	1	6.95	65.4	Washing detergent solution	42.3	0.39
EWDS2	11.50	1	6.95	65.4	Washing detergent solution	42.5	0.34
EMTAS1	11.50	1	6.95	69.3	MTA solution	41.9	0.39
EMTAS2	11.50	1	6.95	69.2	MTA solution	42.9	0.22
EAMPS1	11.50	1	6.95	65.4	AMP solution	39.6	0.03
EAMPS2	11.50	1	6.95	65.4	AMP solution	42.3	0.29
EAMPS3	11.50	1	6.95	65.3	AMP solution	43.3	0.25
EAMPS4	11.50	1	6.95	65.3	AMP solution	44.0	0.07
EAMPS5	11.50	1	6.95	65.3	AMP solution	42.6	0.25
EAMPS6	11.50	1	6.95	65.3	AMP solution	42.4	0.09
EAMPS7	11.50	1	6.95	65.7	AMP solution	41.5	0.43
EAMPS8	11.50	1	6.95	65.7	AMP solution	40.3	0.43
EAMPS9	11.50	1	6.95	65.7	AMP solution	43.6	0.33
EAMPS10	11.50	1	6.95	65.7	AMP solution	40.6	0.42

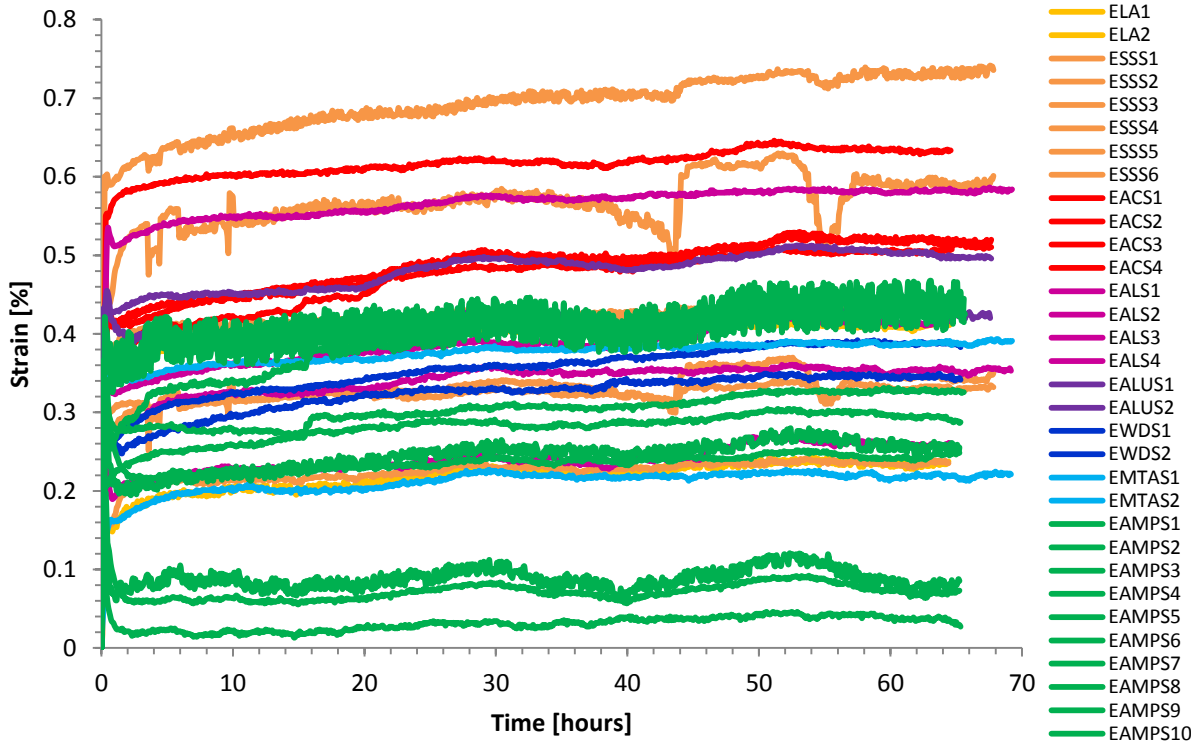

Figure 8: Strain versus time curves for all the experiments performed in Stage II of the Steel Tube experiments. Experiments performed with the same pore fluid are presented in the same colour to aid the recognition of trends, which appears to be absent.

by carefully removing the dead weight. After the assembly length was measured, it was dissembled and the sample was carefully removed from the steel tube and placed in a small cup for dry storage at 50 °C.

2.3.2 Results

In Stage II, 32 experiments were performed, using a large number of different pore fluids. Strain versus time curves of these experiments are presented in Figure 8. In calculating the strain and in constructing the graphs the last 15 minutes of the experiment are not taken into account, in order to avoid disturbance by opening the temperature box. In Figure 8, to facilitate the recognition of trends, experiments performed with the same pore fluid are presented in identical colours. Despite the colours it is difficult to discern trends related to the various pore fluids. However, the AMP solution experiments tend to have lower strain values compared to the other experiments. The solution was therefore tested multiple times to improve the reproducibility and to verify the effect.

To better illustrate some of the experimental results, silica saturated solution experiments and AMP experiments are presented separately in Figures 9 and 10, respectively. The silica saturated solution experiments plot in a broad band, with the final strain ranging from 0.23 % to 0.74 % (see also Table 2). The strain curves of the AMP experiments also plot in a broad band, with final strain ranging from 0.03 % to 0.43 % (see also Table 2). Enlargements of Figures 9 and 10 are presented in Figures 11 and 12, which depict strain data of the first hour of the silica saturated solution and AMP experiments, respectively. In both diagrams, the strain curves have an initial sharp increase in strain, which after a few minutes becomes more gradual. This instantaneous increase is related to the elastic deformation of the entire assembly [10,12,34]. After 10 to 15 minutes (depending on the experiment), a second sharp increase in strain occurs, which

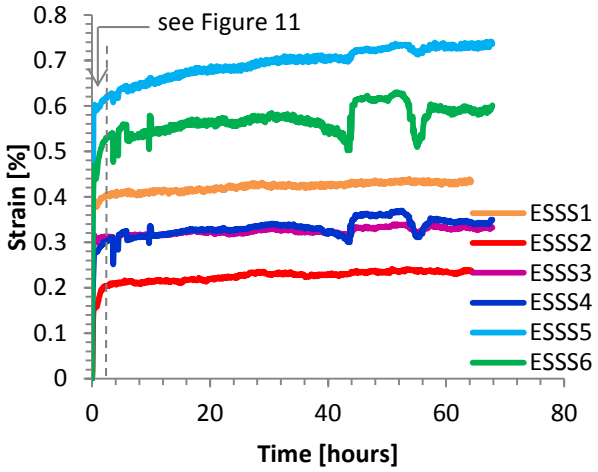

Figure 9: Strain versus time diagram showing the strain curves of the silica saturated solution experiments.

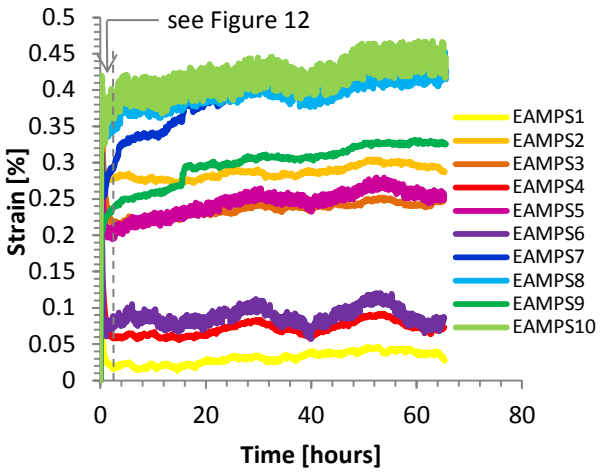

Figure 10: Strain versus time diagram showing the strain curves of the AMP experiments.

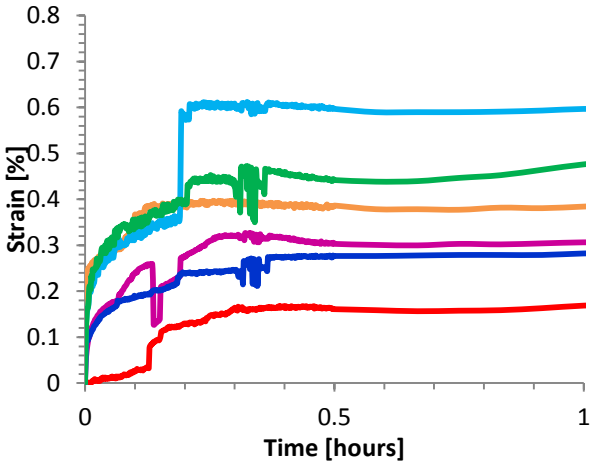

Figure 11: Enlargement of the first hour of Figure 9 showing the effect of adding the pore fluid. Colours same as in Figure 9.

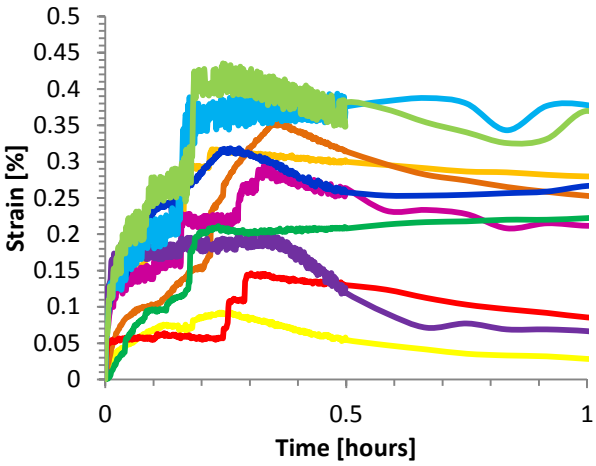

Figure 12: Enlargement of the first hour of Figure 10 showing the effect of adding the pore fluid. Colours same as in Figure 10.

illustrates the effect of adding the pore fluid. Other rises and falls in strain are related to opening and closing the temperature box, as described in Section 2.2.3.2. Strain curves of the other experiments performed with different pore fluids show similar patterns.

2.3.3 Discussion

In Stage II, the type of pore fluid was varied as much as possible in order to find a fluid or multiple fluids that inhibit compaction creep. The results suggest that the AMP solution has an inhibiting effect, but there is a poor reproducibility. The reference cases (lab air and silica saturated solution) are not well constrained and experiments that were supposed to be similar exhibit different compaction behaviours. It is therefore impossible to confidently assess the effect of the various pore fluids. This discussion focusses on the cause of the poor reproducibility and how it can be improved.

Upon closer inspection of the strain curves presented in Figures 11 and 12, it appears that for a large part the final strain is determined by the two sharp strain increases at the start of the experiment. For example, ESSS1 (Figure 11) has 0.40 % strain after approximately 15 minutes

and has a final strain of 0.43 %. In other words, 93 % of the final strain is determined by the two sharp strain increases as the start of the experiment. In a similar study [10], the instantaneous strain accounts for approximately 80 % of the total final strain. It appears that the contribution of the instantaneous strain in this study is rather large, which suggests that something within the assembly interferes the dry compaction.

As possible interfering element is the friction reducing Teflon liner. Upon assembly, it is attempted to completely fill the Teflon with sample material. However, when the length of the sample is determined, it appears to be approximately 1 mm shorter than the length of the Teflon liner. This difference in length can be accommodated in two manners. Firstly, the excess Teflon, which is not filled with sample material, can get squeezed between the walls of the steel tube and the pistons. As a result the Teflon gets stuck, because it is a very tight fit between the pistons and the steel tube. The stuck Teflon will obstruct the movement of the upper piston, which will influence the displacement measured by the gap sensor. The second possibility is that the excess Teflon wrinkles. This could occur at the outer ends of the sample or somewhere halfway. In both cases, the Teflon can form a layer that blocks the movement of the pore fluid and prevents the sample to be uniformly wetted. In addition, a thick wrinkled layer, being very elastic, can significantly contribute to the elastic deformation of the sample. Part of the deformation measured during the experiments could thus be deformation of a wrinkled Teflon layer.

The best way to prevent the disturbance from the Teflon is to perform the experiments without a Teflon liner. However, as explained in Section 2.2.3.1, this will have a negative influence on the experiment. Another solution is to reduce the length of the Teflon liner to a length smaller than the sample length, even after pre-compaction and compaction of the sample. This solution is tried in Stage III. In addition, both outer ends of the sample must not be lined with Teflon. This will ensure the easy entrance of the pore fluid to the sample.

2.4 Stage III: Improving Reproducibility

2.4.1 Testing Procedure

In stage III, each experiment had two phases: pre-compaction and compaction. The samples were pre-compacted dry for approximately 1 hour, using a dead weight of 2355 g (equals a

Table 3: Experimental details of Steel Tube Experiment Stage III

	σ_{pre} [MPa]	t_{pre} [hours]	σ_{comp} [MPa]	t_{comp} [hours]	Pore Fluid	φ_0 [%]	e_v [%]
ESSS7	11.50	1	6.95	24.2	Silica saturated solution	40.1	0.20
ESSS8	11.50	1	6.95	24.2	Silica saturated solution	41.2	0.39
ESSS9	11.50	1	6.95	24.2	Silica saturated solution	41.6	0.48
ESSS10	11.50	1	6.95	24.2	Silica saturated solution	38.6	0.43
ESSS11	11.50	1	6.95	24.2	Silica saturated solution	36.8	0.16
ESSS12	11.50	1	6.95	24.2	Silica saturated solution	41.8	0.25
ESSS13	11.50	1	6.95	24.2	Silica saturated solution	41.1	0.43
ESSS14	11.50	1	6.95	24.2	Silica saturated solution	39.6	0.22
EAMPS11	11.50	1	6.95	23.6	AMP solution	37.5	0.45
EAMPS12	11.50	1	6.95	23.6	AMP solution	38.1	0.22
EAMPS13	11.50	1	6.95	23.6	AMP solution	37.3	0.22
EAMPS14	11.50	1	6.95	23.6	AMP solution	40.1	0.06
EAMPS15	11.50	1	6.95	23.9	AMP solution	40.6	0.22
EAMPS16	11.50	1	6.95	23.9	AMP solution	41.1	0.30
EAMPS17	11.50	1	6.95	23.9	AMP solution	40.3	0.26
EAMPS18	11.50	1	6.95	23.9	AMP solution	37.4	0.44

stress of 11.5 MPa) (Table 3). Dry pre-compaction was performed to obtain an approximately constant starting porosity and a locked aggregate. The subsequent wet compaction phase lasted about 24 hours, during which a dead weight of 1425 g (equals a stress of 6.95 MPa) was used (Table 3).

The experiments were performed using approximately 18 mg of sample material. A Teflon liner (height 5 mm) was placed in the steel tube to minimize the friction between the sample and tube walls. The Teflon height is shorter than the sample length, to minimize the Teflon's influence on the sample's compaction behaviour. To further minimize influences of the Teflon, both ends of the sample were not lined with Teflon (Figure 13). This allows easier fluid access to the sample and ensures that the Teflon does not wrinkle up at the ends.

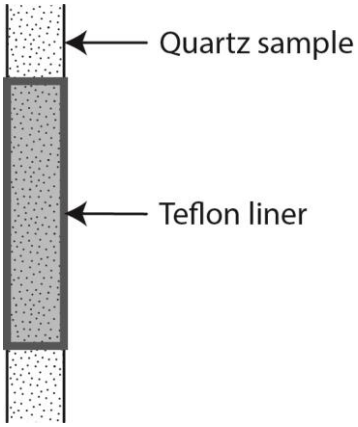

Figure 13: Schematic diagram of sample and the Teflon liner used during Stage III of the steel tubes experiments.

In order to obtain the above described configuration of sample material and Teflon (Figure 13), the sample was funnelled into the steel tube according to the following procedure. First, the bottom piston was inserted in the steel tube and a small quantity of sample material was funnelled in. Before inserting the Teflon liner, it was made sure that no grains were sticking to the tube's wall by carefully inserting the upper piston in the steel tube and pushing the sticking grains down. Next, the Teflon liner was inserted, filled with sample material and a small layer of material was funnelled on top. Lastly, the top piston was put in place and the steel tube placed in the base plate. The assembly was completed by placing the fluid reservoir on top and connecting the evacuation tube. The assembly was tapped multiple times to allow the grains to rearrange, after which the length of the assembly was measured using a calliper.

Subsequently, the pre-compaction weight was placed in the set-up. Accordingly, the height of the gap sensor was adjusted to ensure that at the moment the sample was placed in the set-up, the gap distance (between the sensor and dead weight) would be in the measuring range. The sample was placed in the temperature box and the set-up was left for about 5 minutes to stabilize the temperature. Once the target temperature was reached, the sample was introduced in the set-up by carefully placing it under the dead weight. At the end of the pre-compaction phase, the weight was carefully lifted and the sample was removed. Sample length was again measured using a calliper.

Next, the pre-compaction dead weight was replaced by the compaction dead weight and the gap sensor was adjusted. The box was again closed for several moments to regain temperature. Once temperature was stable, the sample was carefully placed under the dead weight. After about 5 minutes, the selected pore fluid was added to the reservoir. The sample was rapidly flooded by applying a partial vacuum via the evacuation tube. When fluid appeared in the evacuation tube, it was assumed the whole sample was flooded and the tube was closed off. A drop of silicon oil was added to the top reservoir to prevent evaporation of the pore fluid. The experiments were terminated by carefully removing the dead weight. After the assembly length was measured, it was dissembled and the sample was carefully removed from the steel tube and placed in a small cup for dry storage at 50 °C.

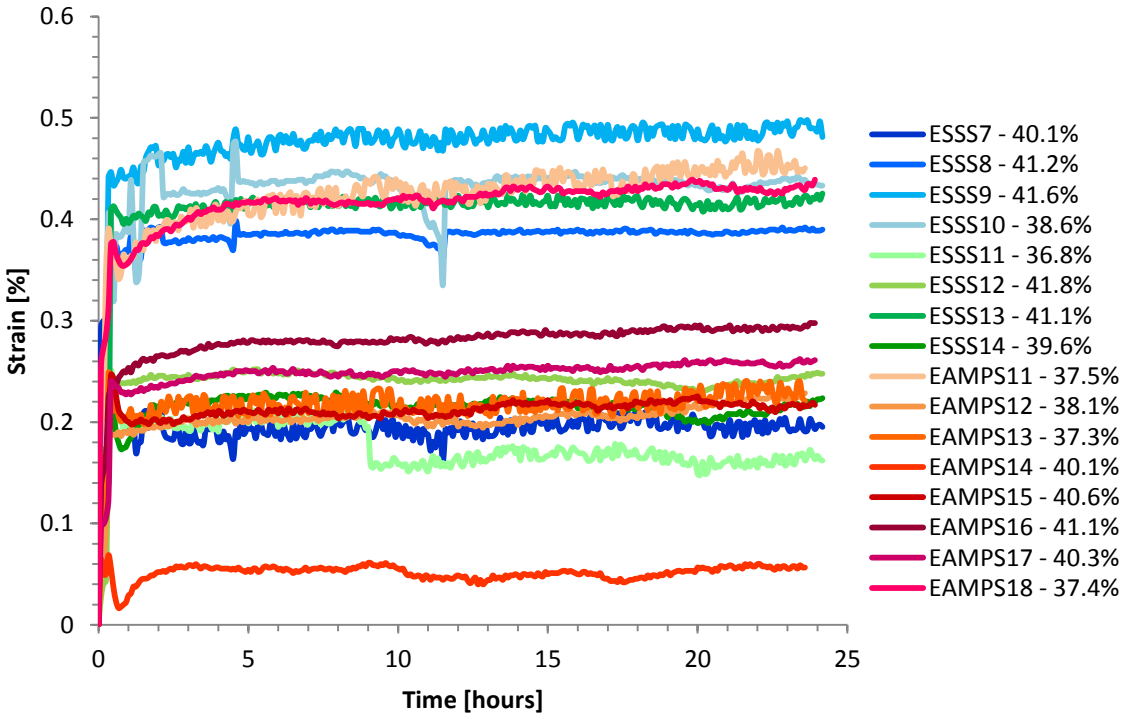

Figure 14: Strain versus time curves for all the experiments performed in Stage III of the Steel Tube experiments. Silica saturated solution experiments are presented in blue and green colours. AMP experiments are presented in red and purple colours. The percentage next to the experiment name indicates the starting porosity of the sample.

2.4.2 Results

During Stage III, 16 experiments were performed. Since Stage II suggested AMP may have an inhibiting effect on compaction creep only two types of pore fluids were used: silica saturated solution and AMP solution. Strain versus time curves of these experiments are presented in Figure 14. The last 15 minutes of the experiments are neither used in the calculations nor in the construction of the graphs to avoid disturbance by opening the temperature box. In Figure 14, two distinct bands of strain curves can be discerned. One band is located around 0.4 % strain and the other around 0.2 % strain. However, the bands do not solely contain one type of pore fluid. On the contrary, the upper band is formed by four silica saturated solution experiments and two AMP experiments. The lower bands also contains strain curves belonging to both silica saturated experiments (four curves) and AMP experiments (five curves). There is one AMP strain curve that plots at very low values.

Trends in the experimental data may become more apparent when a smaller range for the starting porosity is taken. The initial porosity of a sample has a significant influence on compaction creep [10,12,15,34] and the current porosity range (39.3 ± 2.5 %) is too large to avoid this influence. A more reliable porosity range is 40.6 ± 1.0 %. Nine experiments fall into this range and are depicted in Figure 15. Two bands of strain curves are still present, but unlike before, the upper band solely contains silica saturated solution experiments. However, two silica saturated solution curves still plot in the lower band where also the AMP solutions plot. This plot shows that there is a difference in the behaviours of the silica and AMP experiments, but is it not unambiguous. The reproducibility needs to be improved.

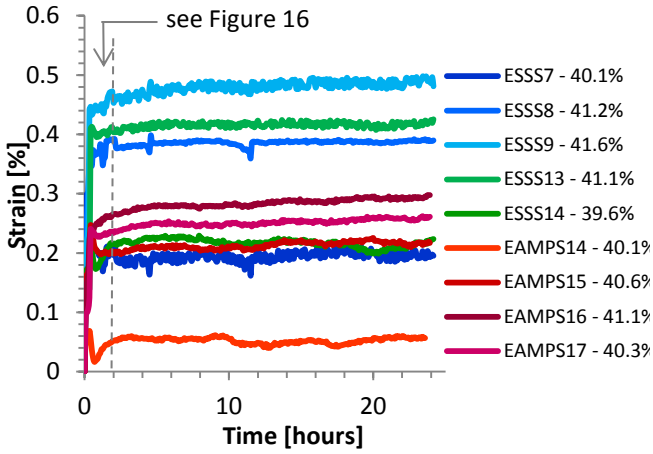

Figure 15: Strain versus time curve showing the silica saturated solution and AMP experiments that fall into the select porosity range of 40.6 ± 1.0 %. The percentage next to the experiment name indicates the starting porosity of the sample.

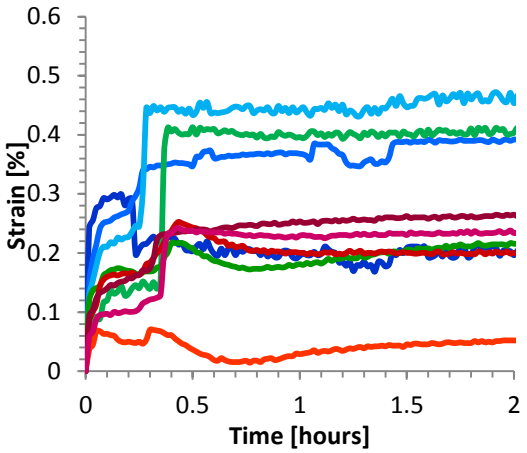

Figure 16: Enlargement of the first two hours of Figure 15 showing the effect of adding the pore fluid. Colours same as in Figure 15.

2.4.3 Discussion

In Stage III, only two pore fluids were tested because of two reasons. Firstly, to verify that AMP has an inhibiting effect on compaction creep, as suggested in Stage II. Secondly, to check the reproducibility of the experiments. The experimental results again suggest that AMP inhibits compaction creep, but it is not conclusive. There is too much variability in both AMP experiments and the baseline experiments (silica saturated solution). In comparison with Stage II, the reproducibility appears to be better, but there is still a need for improvement. Though, this was partly achieved by selecting a narrower porosity range, the initial porosity range remained too large to truly eliminate the effect of starting porosity.

The reproducibility and thus the reliability of the experiments remains limited, even after trying multiple testing procedures and improving the set-up where possible. There could be many causes. For example, the strain and strain rate in the experiments is too low to be accurately measured by the gap sensors. However, in previous studies (e.g. [23]), similar strains were successfully measured using similar gap sensors. Another cause could be the opening and closing of the temperature box. There was an intense response in the recorded voltage signal with every temperature increase or decrease (Figure 16). This problem can be avoided by adding the fluid prior to putting the sample under load or by adding the fluid in a way that does not require the temperature box to be opened. Other causes, could be the Teflon liner, sample size being too large, sample assembly not properly aligned under the dead weight or an askew piston surface that does not transfer the stress uniformly.

However, it is difficult to exactly pinpoint the main cause for the poor reproducibility, making it hard to solve the problem. Therefore, it is decided to abandon this set-up and methodology, and to try similar experiments using another set-up. The trends suggested by the steel tube experiments are used to outline the remainder of this study. The new series of experiments are described in the next chapter.

3 Instron Experiments

In the following, experiments performed using the Instron loading frame and a conventional uniaxial compaction vessel are discussed. This set-up was used, because it gives a better control on the starting porosity. However, as only one experiment can be performed at a time, fewer experiments can be done in total. As with the steel tube experiments, different testing procedures were tried. The Instron experiments are divided in two stages. For each stage the testing procedure, results and discussion are presented. Sample preparation, pore fluid preparation, experimental set-up, and data acquisitioning and processing are discussed first in the general methodology, because these elements remained the same while the testing procedure varied.

3.1 Sample Preparation and General Methods

3.1.1 Sample Preparation

The sample material used in the Instron experiments comes from a large batch of quartz sand of unknown origin. The sand was grinded by hand using a mortar and pestle, and subsequently sieved to a grain size fraction of 212 μm to 250 μm. This specific grain size range was chosen, because it is large enough to be viewed under an optical microscope. With this grain size range, the sample contains more than ten adjacent grains in its diameter. This is necessary to minimalize boundary effects, like friction between the grains and vessel walls.

3.1.2 Pore Fluid Preparation

The Instron experiments were performed using three different pore fluids: lab air, silica saturated solution and silica saturated solution containing 1 ‰ of amino methylene phosphate (AMP). The silica saturated solution was created by dissolving a fixed volume of sodium metasilicate ($Na_2SiO_3 \bullet 9H_2O$) in distilled water. After a thorough stirring, the mixture was diluted to create a solution containing 255 ppm silica. At 25 °C and 0.1 MPa, this is an oversaturated silica solution [25–27]. To create the second solution, a fixed volume of AMP was added to the silica saturated solution. This mixture was also extensively stirred and contained 1 ‰ AMP, in percentage of total solution. AMP is an additive used in a vast variety of industries as scale inhibitor [28–31].

3.1.3 Experimental Set-Up

The Instron experiments were conducted using an Instron 8562 servo-controlled testing machine (Figure 17). The set-up consists of a moveable top piston, a fixed bottom piston and an 1-D (uniaxial) compaction vessel, all made of hardened stainless steel (Remanit 4122). The vessel has a bore of 20 mm in which a smaller vessel can be inserted. This smaller vessel (diameter 10 mm) allows for smaller samples (e.g. less material) and is constructed from Monel K-500, a corrosion-resistant copper-nickel-molybdenum alloy. The Monel vessel also has a matching moveable top and fixed bottom piston made of Monel K-500. Both Remanit and Monel top pistons have a central pore fluid bore and are tipped with a porous plate. This plate ensures uniform distribution of the pore fluid to the sample, and prevent extrusion of sample material into the piston bore. All pistons are sealed with Viton O-rings. Connected to the fluid inlet is a wash-bottle, which is used to vacuum-saturate the sample with pore fluid. During the experiments, the inlet of the wash-bottle remained open to the atmosphere, allowing the pore fluid pressure to be at ambient pressure.

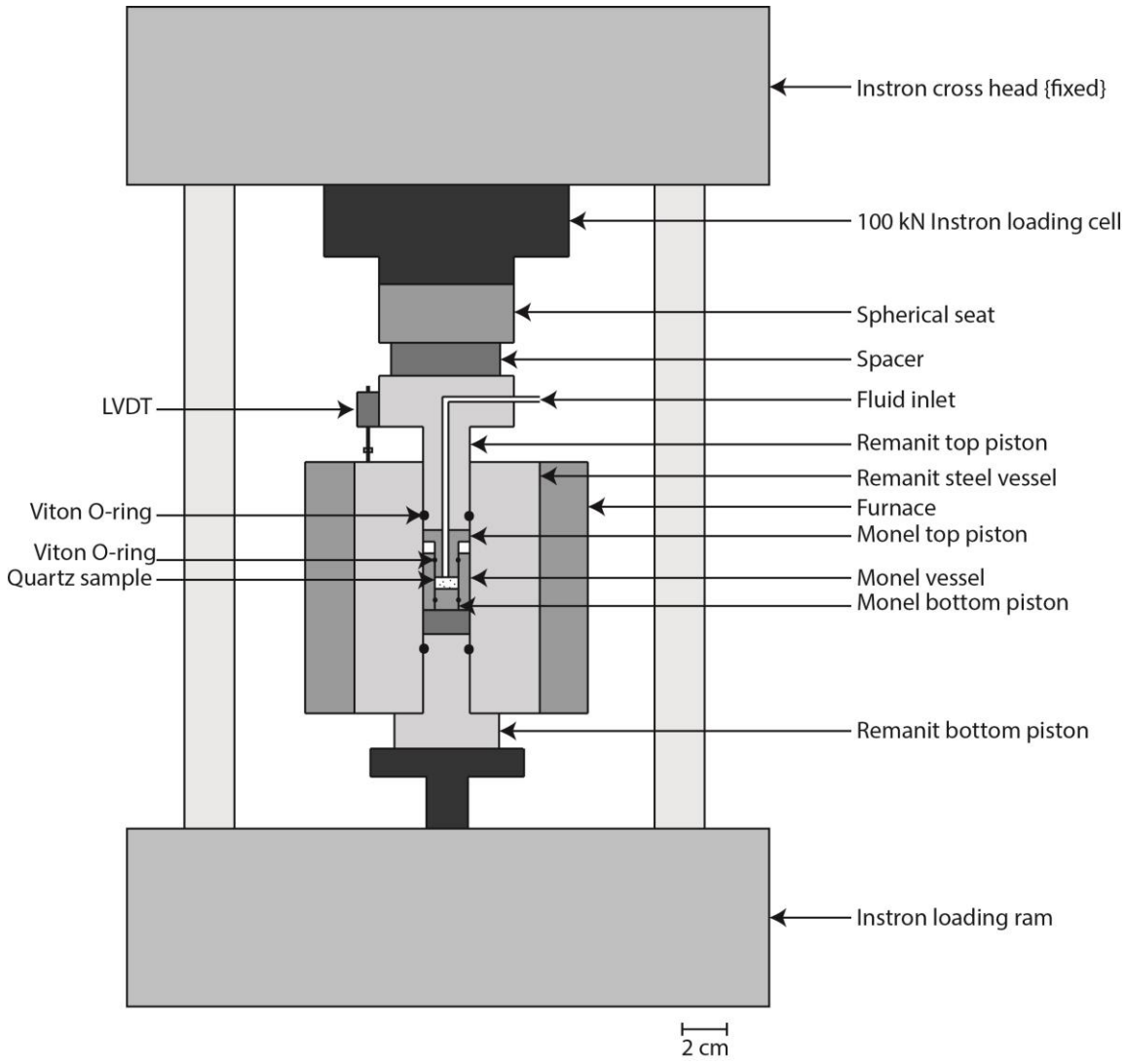

Figure 17: Schematic diagram of the Instron set-up.

The force applied to the top piston is measured externally, using the Instron load cell (100 kN range, resolution ± 0.025 kN). The top piston position and displacement are measured using both the Linear Variable Differential Transformer (LVDT, range ± 50 mm, resolution ±2.5 μm) located in the Instron drive unit and a Solartron LVDT (range ± 1 mm, resolution ± 0.1 μm) that is mounted between the top piston and compaction vessel. The Instron LVDT was used to determine the starting length of the sample, while the Solartron LVDT was used to determine the relative displacement of the top piston with respect to the compaction vessel.

The sample temperature was measured using a thermocouple, which is embedded in the vessel wall close to the sample. To keep the temperature of the complete set-up stable, it is surrounded by a Styrofoam box. The box contains a lamp and fan to maintain a uniform and stable temperature throughout the entire box. The temperature in the box was kept at 30 °C, which was controlled by an Eurotherm temperature controller. A third thermocouple, placed against the steel frame of the Instron, recorded the temperature of the Instron loading frame.

3.1.4 Data Acquisitioning and Processing

Throughout the experiment, applied load, Instron LVDT position, Solartran LVDT position, pore fluid pressure, sample temperature, Instron temperature and box temperature were logged

every second using a 16-bit NI DAQPad-6015 A/D converter. The resolution of the Instron load was optimized for the range 0 kN to -20 kN. To correct for the elastic distortion in the set-up, a calibration was performed using the Monel vessel (without sample) as a dummy. Various loads were applied and the associated displacement was recorded. A least-square fit was made to the data and the formula describing this linear line allowed to correct for elastic distortion in the system at any given load.

After the elastic distortion correction was applied sample length, volumetric strain, volumetric strain rate and porosity could be calculated as a function of time. The starting point for all the calculations was chosen to be the first moment in time when the applied load equalled the intended compaction load. In uniaxial experiments, the instantaneous volumetric strain $e_v = -\frac{\Delta V}{V_0}$ equals the instantaneous axial strain $e_v = -\frac{\Delta L}{L_0}$, because the sample can only deform along its length. Instantaneous strain rates, defined as $\dot{\varepsilon} = -\frac{1}{L}\frac{dL}{dt}$, were calculated by performing a least-squares regression to the displacement versus time data, using a moving displacement interval.

3.2 Stage I: Dry Pre-Compaction Prior to Fluid Addition

3.2.1 Testing Procedure

The testing procedure of Stage I of the Instron experiments is similar to the testing procedure of the steel tube experiments in the sense that the samples are first pre-compacted at a high stress and then compacted at a lower stress.

The experiments were performed using approximately 0.65 g of sample material. Before the sample was funnelled into the Monel vessel, a Teflon liner (height approximately 3 mm) was placed in the vessel to reduce friction between the sample and vessel walls. The ends of the Teflon liner were taped close (forming a cylinder), so upon retrieval the sample would remain intact. The Teflon height is shorter than the sample length, to minimize the Teflon's negative influence on the sample's compaction behaviour. After introduction of the sample, the top Monel piston was inserted and the vessel was tapped multiple times to allow grain rearrangement.

Next, the Remanit bottom piston and compaction vessel were put in place. A small Monel spacer was inserted in the compaction vessel to provide enough length for the Remanit top piston to touch the Monel top piston. Subsequently, the Monel assembly was carefully placed in the Remanit vessel and the Remanit top piston was inserted. After placing a spacer on the Remanit top piston, connecting the wash-bottle filled with the appropriate fluid, and connecting the fluid tubes, the system was left to stabilize the temperature for one hour. Once a stable box temperature (30 °C) and sample temperature (25 °C) was obtained, the loading ram was, in position control, gently brought to touch.

Table 4: Experimental details of Instron Experiments Stage I

	σ_{pre} [MPa]	t_{pre} [hours]	σ_{comp} [MPa]	t_{comp} [hours]	Pore Fluid	φ_0 [%]	e_v [%]
ISSS1	45	1	35	18.2	Silica saturated solution	31.2	0.43
ISSS2	45	23	35	16.2	Silica saturated solution	33.6	0.37
ISSS3	45	5	35	15.8	Silica saturated solution	33.9	0.36
ISSS4	45	5	35	14.4	Silica saturated solution	33.5	0.41
ISSS5	45	5	35	36.9	Silica saturated solution	32.1	0.35
IAMPS1	45	5	35	17.8	AMP solution	33.7	0.40

After touch, the machine was switched to load control and in 60 seconds the load was increased lineraly to the pre-compaction load of -3.53 kN (equals 45 MPa stress). Pre-compaction lasted at least five hours (Table 4) to ensure that the sample formed a locked aggregate. The first experiment (ISSS1) is an exception, because initially it was assumed that one hour would be sufficient to form a locked aggregate. Pre-compaction was terminated by reducing the load to a load similar to the load at touch. Next, the experiments were evacuated using a vacuum pump that was connected to the wash-bottle. After about 15 minutes of evacuation, the vacuum was released, forcing the fluid to move quickly into the system and sample. The compaction phase was commenced by linearly increasing the load in 60 seconds to -2.75 kN (equals 35 MPa stress). The load was kept constant and sample displacement was measured for approximately 24 hours (Table 4).

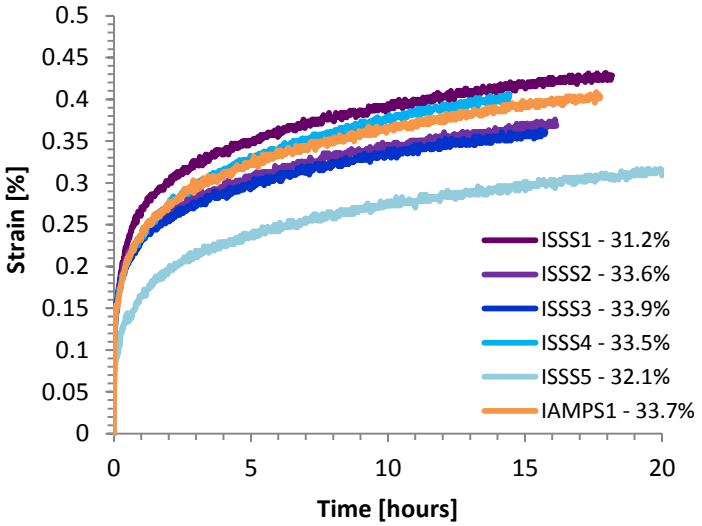

Figure 18: Strain versus time diagram showing the compaction creep curves of Stage I of the Instron experiments. The percentage next to the experiment name indicates the starting porosity of the sample.

The experiments were terminated by decreasing the applied load to a load similar to the load at touch. Next, the system was switched into position control and the loading ram was further retracted until the sample was fully unloaded. The set-up was dissembled by disconnecting the fluid tube and removing the wash-bottle, spacer and Remanit top piston. After draining the fluid from the compaction vessel, the Monel vessel was carefully removed. The Monel top piston was removed and the sample carefully slid in a small container for dry storage at 50°C. The samples were retrieved completely wet and intact.

3.2.2 Results

In Stage I of the Instron experiment, six experiments were performed. One experiment had AMP solution as pore fluid, the pore fluid of the other experiments was silica saturated solution. In Figure 18, strain versus time curves of these experiments are presented. The silica saturated experiments plot in a narrow range of less than 0.1 % strain (see also Table 4). An exception is ISSS5, which plots at lower strain values. The AMP experiment plots among the silica saturated solution experiments as if it was performed with the same pore fluid. Unlike the results from the steel tube experiments, these results suggest that an AMP solution does not influence compaction creep differently than a silica saturated solution.

3.2.3 Discussion

The aim of Stage I was to test and try the Instron set-up and to verify the effect of AMP on compaction creep as suggested from the steel tube data. However, the data obtained during this stage indicates that AMP does not influence compaction creep. The lack of difference between the silica saturated experiments and the AMP experiment could be related to the pre-compaction phase. Initial pre-compaction with a high load could create a locked aggregate by failure of the critically stressed grain flaws. During subsequent compaction with a smaller load,

there are just a few critically stressed grain flaws, inducing only minor deformation. If the difference between the pre-compaction and the compaction load is too large, even sub-critical flaws cannot become critical with the addition of a fluid during the compaction phase (refer to Section 3.3.3.2 for further explanation). Furthermore, the effect of adding a creep inhibiting fluid would also be small and difficult to discern. This would result in experiments with different chemical environments behaving similarly.

To avoid pre-compaction having a larger influence on creep behaviour than the chemical environment, the samples are not pre-compacted during the next stage. Instead, each sample is crushed to a set porosity, resulting in a well-controlled starting porosity.

3.3 Stage II: No Pre-Compaction, Controlling Starting Porosity

3.3.1 Testing Procedure

The first steps of the testing procedure of Stage II are similar to Stage I. Refer to Section 3.2.1 for a description of the sample assembly and the introduction of the assembly into the Instron loading frame.

After sample assembly and introducing the sample into the Instron loading frame, the loading ram was, in position control, gently brought to touch. Subsequently, the sample was step-by-step crushed to a set starting length in order to obtain a fixed starting porosity of 35.5 ± 0.6 % (Table 5). The load applied during crushing was not allowed to exceed the load applied during the creep phase (Table 5). Next, the samples (except for the lab air experiments) were evacuated using a vacuum pump that was connected to the wash-bottle. After about 15 minutes of evacuation, the vacuum was released, forcing the fluid to move into the system and thereby rapidly flooding the sample, i.e. vacuum saturating. Subsequently, the system was switched to load control and in 60 seconds the load was increased linearly to -2.75 kN (equals a stress of 35 MPa). While maintaining the load, sample deformation was measured for about a day.

The experiments were terminated by decreasing the applied load to a load similar to the load at touch. Next, the system was switched into position control and the loading ram was further retracted until the sample was fully unloaded. The set-up was dissembled by disconnecting the fluid tube and removing the wash-bottle, spacer and Remanit top piston. After draining the fluid from the compaction vessel, the Monel vessel was carefully removed. The Monel top piston was removed and the sample carefully slid in a container for dry storage at 50 °C. The wet samples

Table 5: Experimental details of Instron Experiments Stage II

	$\sigma_{\text{crush, max}}$ [MPa]	σ_{comp} [MPa]	t_{comp} [hours]	Pore Fluid	φ_0 [%]	e_v [%]
ILA1	24.44	35	19.4	Lab air	35.4	0.84
ILA2	30.35	35	46.3	Lab air	35.4	0.92
ILA3	31.01	35	20.7	Lab air	35.0	0.94
ISSS6	25.30	35	44.6	Silica saturated solution	36.1	1.13
ISSS7	25.14	35	20.0	Silica saturated solution	35.9	1.43
ISSS8	28.79	35	42.8	Silica saturated solution	35.6	1.21
ISSS9*	30.93	35	19.2	Silica saturated solution	34.7	0.81
ISSS10	16.75	35	22.1	Silica saturated solution	34.9	1.15
IAMPS2	20.48	35	16.4	AMP solution	35.0	0.91
IAMPS3	28.02	35	19.0	AMP solution	35.2	0.81
IAMPS4	14.77	35	19.4	AMP solution	35.0	0.90
IAMPS5*	45.11	35	40.8	AMP solution	33.7	0.37

* excluded from results, due to porosity and/or crushing load not meeting set requirements.

were retrieved completely wet and intact, while the dry samples had no cohesion and fell apart in the container.

3.3.2 Results

3.3.2.1 Lab Air

Three experiments using lab air as pore fluid were performed. As shown in Figure 19, the lab air experiments have a good reproducibility. ILA1 and ILA2 have the same starting porosity of 35.4 % and have similar strain versus time curves. Compared to ILA1 and ILA2, ILA3 has a slightly lower porosity (35.0 %) and exhibits slightly more strain. After 15 hours of compaction, ILA1, ILA2 and ILA3 experienced comparable strains of 0.81 %, 0.74 % and 0.89 %, respectively. The strain rates of the three experiments evolve alike with increasing strain (Figure 20). At low strain values, ILA1 shows strain rates equal to ILA3, while at high strain values, ILA1 becomes more similar to ILA2. At 0.7 % strain, ILA1, ILA2 and ILA3 have strain rate values of 10^{-8} s^{-1}, 10^{-8} s^{-1} and 10^{-7} s^{-1}, respectively. In other words, ILA1 and ILA2 deform at the slowest rate, while ILA3 deforms at the fastest rate.

3.3.2.2 Silica Saturated Solution

Five silica saturation solution experiments were performed, but one experiment (ISSS9) did not meet the set requirements (Table 5). As shown in Figure 21, three out of the four experiments have similar results. The strain curves of ISSS6, ISSS8 and ISSS10 evolve similar with time and after 15 hours they experienced 1.00 %, 1.03 % and 1.06 % strain, respectively. ISSS7, on the other hand, shows higher strains during the whole of the experiment and after 15 hours experienced 1.37 % strain. The same trend is visible in the strain rate curves (Figure 22), where ISSS6, ISSS8 and ISSS10 plot more or less the same, while ISSS7 appears to be an outlier. Also, at 0.7 % strain, the strain rates of ISSS6, ISSS8 and ISSS10 are alike, 10^{-7} s^{-1}, 10^{-7} s^{-1} and 10^{-7} s^{-1}, respectively, while ISSS7 has a different strain rate of 10^{-6} s^{-1}. This indicates that ISSS7 deforms at a higher rate than the other silica saturated solution experiments.

3.3.2.3 AMP Solution

Four experiments using a silica saturated solution with 1 ‰ AMP as pore fluid were performed, but one experiment (IAMPS5) did not meet the set requirements (Table 5). As shown in Figure 23, the AMP experiments have a good reproducibility. While IAMPS2 and IAMPS3 have the same starting porosity of 35.0 %, they have slightly different strain curves. IAMPS4, on the other hand, has a different starting porosity (35.2 %) and its strain curve is similar to IAMPS2. Nevertheless, after 15 hours of compaction, the IAMPS2, IAMPS3 and IAMPS4 obtained similar strain values of 0.90 %, 0.78 % and 0.87 %, respectively. A matching trend can be discerned from the strain rate curves (Figure 24). The strain rate curves of IAMPS2 and IAMPS4 are alike, while IAMPS3 has lower strain rates at similar strains. At 0.7 % strain, IAMPS2 and IAMPS4 have a strain rate of 10^{-7} s^{-1} and 10^{-7} s^{-1} respectively. It was impossible to calculate the strain rate of IAMPS3 at 0.7 % strain in the conventional manner, because the amount of sample deformation was smaller than the displacement window defined to calculate the strain rate. However, the data at smaller strains can be extrapolated, resulting in a strain rate of 10^{-8} s^{-1}.

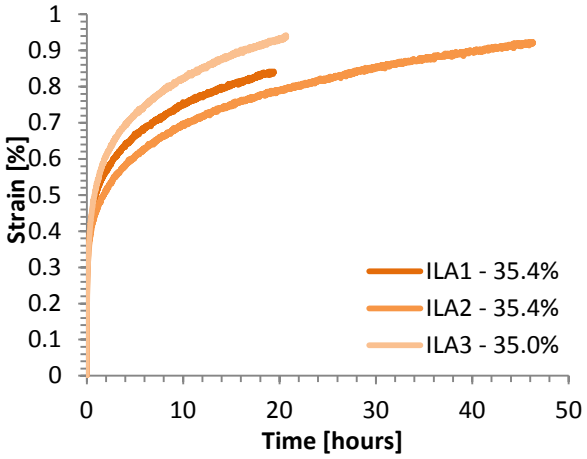

Figure 19: Strain versus time diagram showing the creep curves of the lab air experiments. The percentage next to the experiment name indicates the starting porosity of the sample.

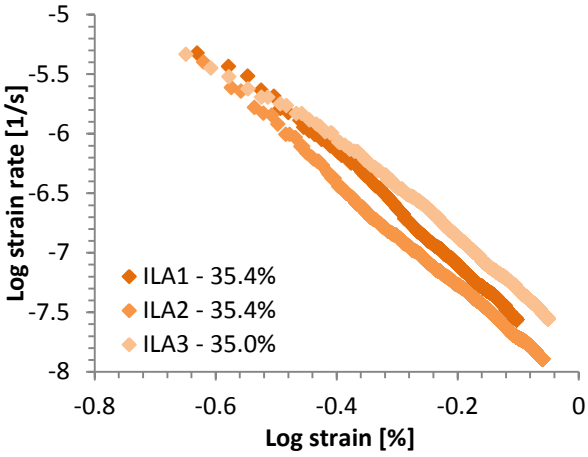

Figure 20: Log strain rate versus log strain diagram showing the strain rates of the lab air experiments, as derives from Figure 19. The percentage next to the experiment name indicates the starting porosity of the sample.

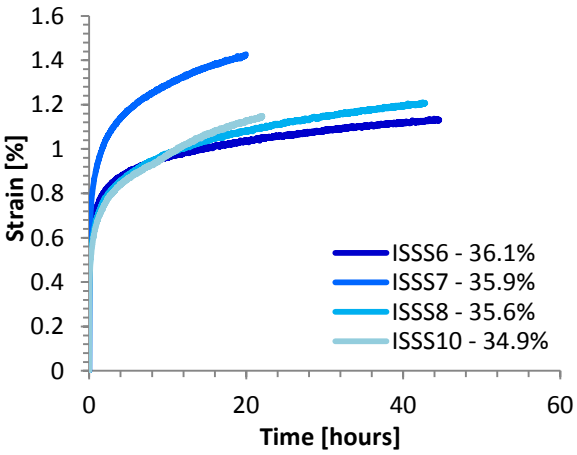

Figure 21: Strain versus time diagram showing the creep curves of the silica saturated solution experiments. The percentage next to the experiment name indicates the starting porosity of the sample.

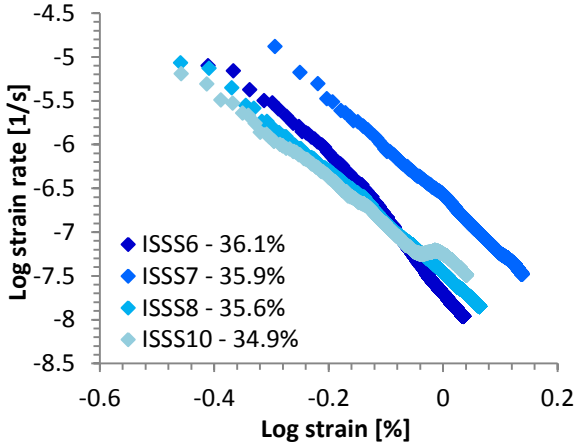

Figure 22: Log strain rate versus log strain diagram showing the strain rates of the silica saturated solution experiments, as derived from Figure 21. The percentage next to the experiment name indicates the starting porosity of the sample.

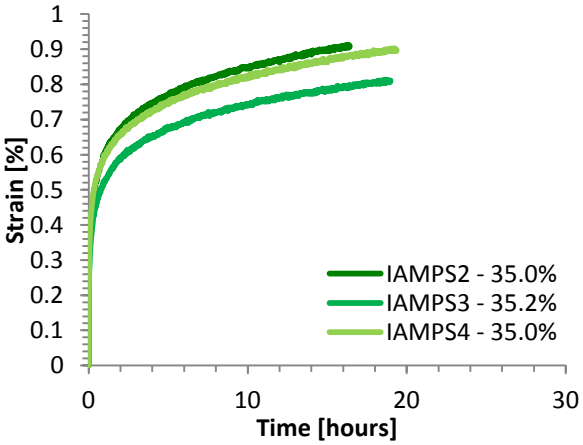

Figure 23: Strain versus time diagram showing the creep curves of the AMP experiments. The percentage next to the experiment name indicates the starting porosity of the sample.

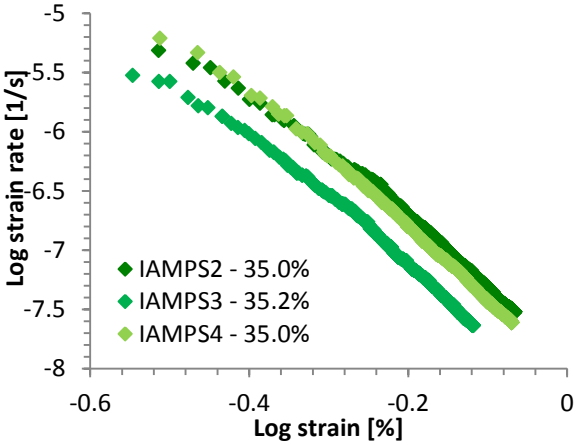

Figure 24: Log strain rate versus log strain diagram showing the strain rates of the AMP experiments, as derived from Figure 23. The percentage next to the experiment name indicates the starting porosity of the sample.

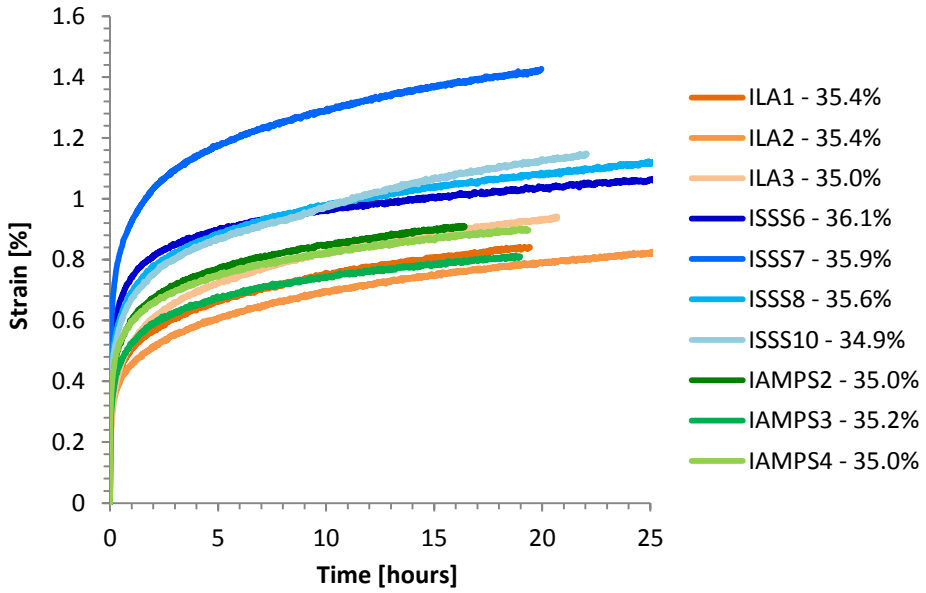

Figure 25: Strain versus time diagram showing the strain curves of all the Instron experiments performed in Stage II. Compared to the lab air experiments, the silica saturated solution experiments have higher strains, while the AMP experiments have similar strains. The percentage next to the experiment name indicates the starting porosity of the sample.

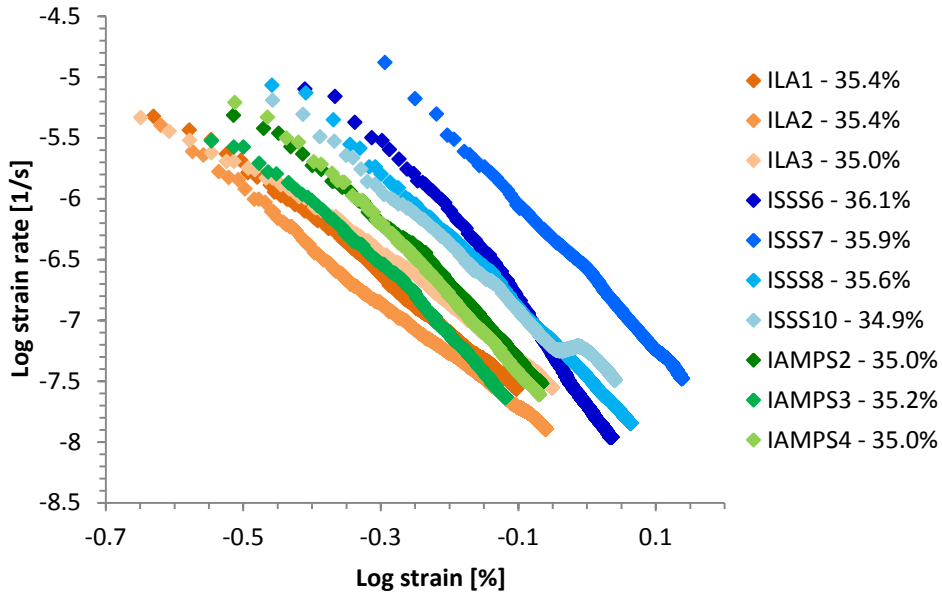

Figure 26: Log strain rate versus log strain diagram showing the strain rates of all the Instron experiments performed in Stage II. Overall, the silica saturated solution experiments have the highest strain rates, while the strain rates of both lab air and AMP experiments are slower. The percentage next to the experiment name indicates the starting porosity of the sample.

3.3.2.4 Effect of Chemical Environment on Creep

By comparing the results of the various pore fluid experiments to the reference experiments (i.e., lab air experiments), the effect of chemical environment on creep behaviour can be deduced. This is done by compiling combination plots of strain versus time (Figure 25) and log strain rate versus log strain (Figure 26). In addition, two diagrams have been constructed to aid the comparison. One displays the strain for each experiment at three chosen moments in time (Figure 27) and the other depicts the strain rate of each experiment at four chosen amounts of strain (Figure 28).

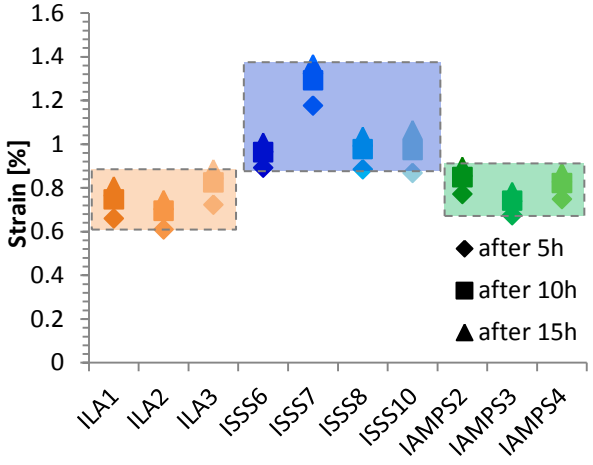

Figure 27: Diagram showing the amount of strain per experiment at three moments in time: after 5, 10 and 15 hours into the experiments.

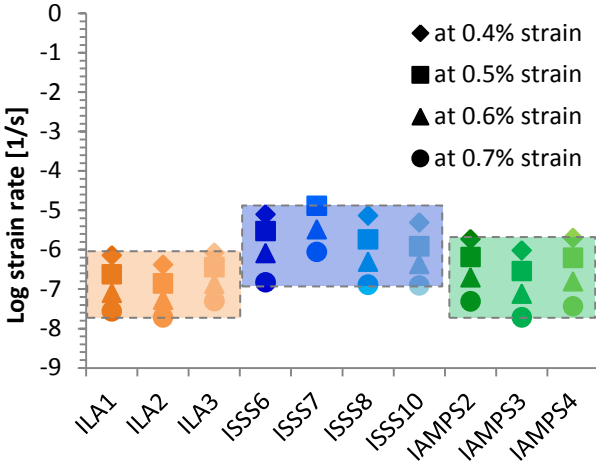

Figure 28: Diagram showing the log strain rate per experiment at four selected strain values: 0.4, 0.5, 0.6 and 0.7 % strain.

Firstly, the effect of a silica saturated solution on creep is investigated. Figure 25 shows that the silica saturated solution experiments experience more strain during compaction that the lab air experiments. This effect also apparent in Figure 27. In this diagram, all silica saturated solution data plot higher than the lab air data. Already after five hours of compaction, the amount of strain in the silica saturated solution experiments is higher than strain in the lab air experiments after 15 hours of compaction (except for ILA3). In Figure 26, the silica saturated solution data forms its own distinct cluster of curves, which is located at higher strains and strain rates compared to the lab air data. The high strain rates are even more apparent in Figure 28, which shows that at each given strain value the strain rate of the silica saturated solution experiments are higher than the strain rates of the lab air experiments.

Secondly, the effect of adding 1 ‰ AMP to the silica saturated pore fluid on creep is investigated. In Figure 25, the AMP experiments strain curves plot among and at slightly higher strain than the lab air experiments curves. This indicates that the AMP solution experiments behave similar to the lab air experiments. Figure 27 also illustrates this effect. At the various moments in time, the AMP solution experiments have similar (some slightly higher) strain values as the lab air experiments.

In Figure 26 similar observations can be made. Initial the strain rates of the AMP experiments are higher than the lab air experiments, but as compaction progresses the AMP experiments become slower. At a log strain of approximately -0.25 % ($e \approx 0.6$ %), there appears to be small change in slope of the AMP solution data. At log strain values lower than -0.25 %, the slope in the AMP data is similar to the lab air slope, while at values higher than -0.25 % the slope is steeper, because it quickly drops to lower strain rates. In other words, at high strain the deformation rate of the AMP experiments becomes slower. This observation is consistent with the results presented in Figure 28. The diagram illustrates an increase in the distance between the AMP data points with increasing strain, while the distance between the lab air experiments data points remain the same with increasing strain.

3.3.3 Discussion

The result from Stage II proved to be reproducible and the experiments are regarded as successful. This discussion will therefore not focus on the methodology, but on the aims of this

study: 1) understanding compaction mechanisms; and 2) investigating the effect of fluids on compaction behaviour. The discussion starts with an analysis of the time-independent and time-dependent mechanisms that controlled compaction during the experiments. This is followed by an exploration into causes of the observed effects of the tested pore fluids.

3.3.3.1 Compaction Mechanisms

Within the first few minutes, all experiments showed rapid and instantaneous compaction, also known as time-independent deformation. This was followed by time-dependent deformation, which is characterized by a gradually increasing strain (creep).

At the experimental temperature and pressure conditions, time-independent deformation could be caused by various compaction mechanisms: 1) grain rearrangement through intergranular sliding and rolling; 2) elastic distortion of grains and grain contacts; 3) failure of grains and grain contacts due to the propagation of pre-existing cracks or flaws [10,12,34]. The first mechanism, grain rearrangement, accommodated by intergranular sliding and rolling, is active until a locked aggregate is created. This mechanism produces only small strains, which are dependent on the starting porosity [12,14,34]. In the current experiments, prior to applying the compaction load, the samples were crushed to a set starting porosity, which most likely created a locked aggregate. This leaves little room for further grain rearrangement. The second mechanism, elastic distortion, only has a small contribution to the instantaneous compaction because of two reasons. First, elastic deformation of grains and grain contacts can only result in very small strains. Secondly, the start of the experiments is at load, hence the elastic deformation should have occurred already. The third mechanism, grain and grain contact failure, is able to create larger strains. In previous studies (e.g. [10,12,14,34]), microstructural analysis and acoustic emission data showed the widespread occurrence of grain cracking. Therefore, it is inferred that grain rearrangement and grain scale microcracking are the main controlling mechanisms during time-independent compaction.

Possible mechanisms active during time-dependent deformation include: 1) dissolution at grain contacts due to undersaturation of the pore fluid with respect to the solid; 2) pressure solution at grain contacts; 3) subcritical crushing at grain contacts; and 4) subcritical, grain scale microfacturing [10,14,35–38]. Both dissolution and pressure solution are expected to have a minor contribution to compaction creep. Strain rate calculations (Appendix A) based on the pressure solution model of [39] for a simple cubic pack of spherical quartz grains, yield dissolution and pressure solution strain rates in the order of 10^{-14} s^{-1}. These are 6-9 orders of magnitude slower than the creep rates measured in these experiments (Figures 26 and 28). Therefore, it is inferred that the creep controlling mechanisms are subcritical fracturing of grains and grain contacts with subsequent rearrangement of grains and grain fragments.

3.3.3.2 Effect of silica saturated solution on compaction

The inferred controlling mechanism for time-independent compaction is microcracking. In crystalline material (e.g. quartz grains), microcracking occurs via the growth of cracks and surface flaws. A crack grows when the stresses that concentrate around the crack tip reach a critical stress state and satisfy the Griffith criterion for crack growth [40]. Similarly, surface flaws located in the margin of grain contacts can become critically stressed [34,41]. Based on the Hertzian contact theory [34,41,42], the contact force (*F)* required to break a spherical grain of diameter (*d)* can be determined from the following grain failure criterion

$$F = \frac{Ad^2}{c^{3/2}} \cdot K_{IC}^3 \quad (1)$$

where A is a constant for the elastic properties of the grain (i.e. Young's modulus and Poisson's ratio), c is the mean flaw half-length, and K_{IC} is the fracture toughness or critical stress intensity factor [10,34,41]. The fracture toughness of a mode I opening crack can be further defined as

$$K_{IC} = \sqrt{\frac{2E\gamma}{1-\upsilon^2}} \quad (2)$$

where E is the Young's modulus of the solid, γ is the solid's surface energy and υ is its Poisson's ratio [10,43]. From equation (1) and (2), it can be deduced that a reduction in the surface energy lowers the fracture toughness and hence reduces the force required to break a grain.

In a dry environment, strongly bonded siloxane groups ($\equiv Si - O - Si \equiv$) make up the surface of a quartz grain [44–46]. However, introduction of water produces weaker, hydrogen bonded, silanol groups ($\equiv Si - OH$), via a hydrolysis reaction

$$\equiv Si - O - Si \equiv + H_2O \leftrightarrow \equiv Si - OH \bullet HO - Si \equiv \quad (3)$$

where • depicts the weak hydrogen bond [44–46]. As a result, the surface energy of the quartz grains is reduced [44–46]. Compared to the strongly bonded siloxane groups, the weakly bonded silanol groups are more prone to rupture, because less energy is require to break the bond. Accordingly, in the silica saturated experiments, a lower force is required to fracture the grains, resulting in high instantaneous strains.

A similar reasoning can explain the high strains of the silica saturated solution experiments observed during the creep stage. The inferred deformation mechanism during creep is subcritical crack growth. Subcritical crack growth is the process were a crack may form and grow at tensile stresses far below the critical stress required to break a grain [46,47]. A crack propagates via the rupturing of $Si - O$ bonds at crack tips [46]. In a wet environment, the silanol bonds allows bond rupture to occur at even lower stress, accelerating the rupture rates and promoting subcritical crack growth. This process is classically described as stress-corrosion cracking [44–46]. In the silica saturated experiments, this effect is illustrated by the higher strains and higher strain rates, compared to the dry experiments.

3.3.3.3 Effect of AMP on compaction

Unlike the silica saturated solution experiments, the AMP experiments showed low strains and low strain rates, similar to the dry experiments. This indicates that though the AMP experiments were wet, stress-corrosion cracking was inhibited. The AMP molecules somehow inhibit wetting of the crack tips.

AMP is in many industries used as an additive to inhibit the formation of scale [29–31]. The AMP molecules adsorb onto crystal surfaces of insoluble salts and prevents further crystal growth [31,48]. In a similar fashion, AMP is envisioned to adsorb to the surfaces of quartz grains and cracks. Having a relatively large and rigid molecule [30,31,48], AMP can obstruct the entrance to the crack tip and inhibit water to enter the crack (Figure 29). As a result, the crack tip remains drier and hydrolysis of strongly bonded siloxane groups is inhibited. Adsorption of AMP to the crack surfaces is not likely to occur instantaneously and the molecule is not likely to close the

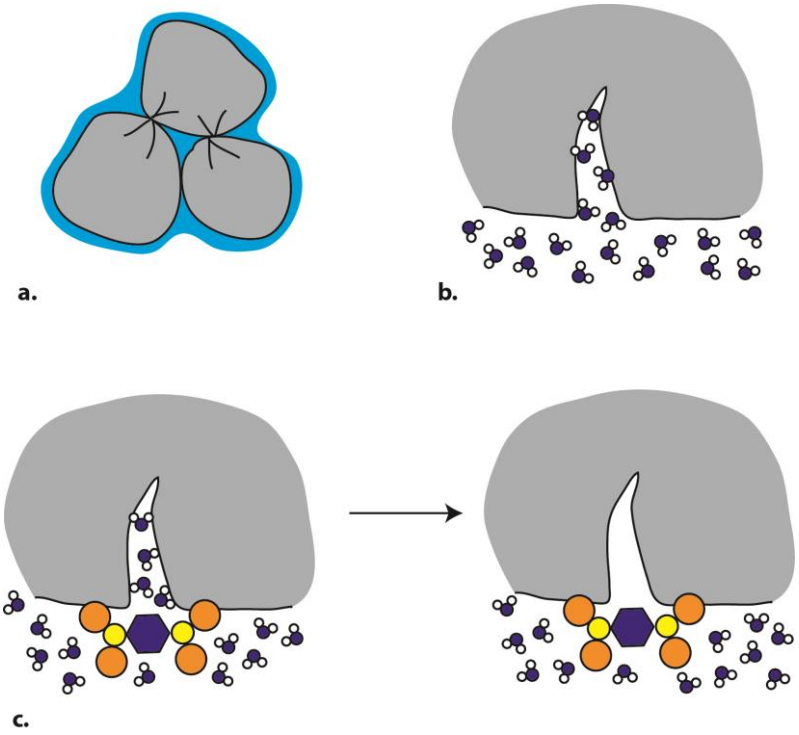

Figure 29: Schematic diagram illustrating the effect of AMP, not to scale. In an aggregate of quartz grains, where the pores are filled with water (a), microcracks radiating from the grain contacts are also filled with water (b). When the AMP is added to the pore fluid, the AMP molecule adsorb to the surface of the quartz grains, thereby blocking the entrance to the crack (c). As the water present in the crack tip is consumed during hydrolysis of the Si-O bonds at the crack tip and the AMP molecule prevents other water molecules to enter the crack, the crack eventually becomes drier.

crack completely. Consequently, some water will enter the crack, leading to minor hydrolysis of the Si – O bonds at the crack tip. As shown in the preceding section, the hydrolysis reaction consumes water to break bonds, and the little water present in the crack will be consumed, resulting in a relatively dry crack (Figure 29).

This theory is consistent with the observed results. Initially, the AMP experiments have strains and strain rates larger than the lab air experiments (Figures 25-28). This reflects stress-corrosion cracking due to the water present in the crack tips. After approximately an hour, the strain rates of the AMP experiments decrease and become more similar to the lab air experiments (Figures 26 and 28). At this stage, it is inferred that the water initially present in the cracks is consumed and the AMP molecules blocking the crack entrance deter further stress-corrosion cracking.

4 Calculating Reservoir Compaction

In the previous chapters, the compaction of sands was studied in order to get a better understanding of the processes and mechanisms at work during compaction creep. In this chapter, compaction is regarded at the reservoir level. When the volume of a producing reservoir decreases as a result of depletion-induced reservoir compaction it can cause seismicity and surface subsidence, which is discussed in the next chapter. However, before the seismic hazard and surface subsidence can be determined, it must be understood how reservoir compaction is generally calculated and which parameters are involved in the calculation. In the following, a brief explanation is provided.

4.1 Reservoir Compaction

When the pressure in the reservoir decreases, the effective stress increases and the reservoir compacts. Reservoir compaction is a reduction in reservoir volume, which is primarily the result of a reduction in reservoir height [49]. The thickness of a reservoir is very small compared to the lateral extend of the reservoir. As a consequence, an increase in effective stress predominantly results in a deformation in the vertical plane. Assuming a linear rheology, the vertical strain caused by an increase in effective stress due to a reduction in reservoir or pore pressure under constant overburden is given by

$$e_z = c_m \Delta P \tag{4}$$

where c_m is the uniaxial compaction coefficient, which is a measure of the compressibility of the reservoir, and ΔP is the reduction in pore fluid or reservoir pressure [17,49]. The total reduction of the reservoir height can be expressed as

$$\Delta H = \int_0^H c_m(z) \Delta P(z)\, dz$$

This equation shows that there are three elements that influence reservoir compaction: 1) the reduction in the reservoir pressure, 2) the vertical extent of the zone where pore pressure reduction takes place, and 3) the compressibility of the reservoir rock [49].

4.2 Rock Compressibility

In modelling reservoir compaction, reduction in the reservoir pressure and the height of the pressure reduction zone are relative well constrained by measurements from wellbores. The compressibility, on the other hand, is not well constrained, because it needs to be determined experimentally. This can be done by uniaxial, triaxial or hydrostatic experiments [17,18,49]. There are multiple sources of experimental error, for example, the selection of representative material, core damage [50], experimental design [16,49] and the use of equations to relate parameters [16,17]. From the experiments, the uniaxial compaction coefficient is calculated according to

$$c_m = \frac{1}{V_b}\left(\frac{dV_b}{dP_p}\right)_{\Delta P_c = 0}$$

where V_b is bulk volume or outer volume of the sample, P_p the pore fluid pressure and P_c the confining pressure, which is the pressure imposed on the rock by the overburden. In other

words, the uniaxial compaction coefficient is the formation compaction per unit change in pore pressure reduction at constant confining pressure.

4.3 Poroelasticity

In porous rock, like the reservoir rock in the Groningen field, the pores are filled with fluid which interacts with the solid rock matrix. This interaction is described by the theory of poroelasticity [51]. The compressibility measured in the experiments (i.e. bulk rock compressibility) is the sum of the pore compressibility and the matrix compressibility. While the bulk compressibility can be used to predict the amount of reservoir compaction at a certain pressure change, pore volume compressibility is an important parameter to predict the reduction in porosity and permeability.

Rock compressibility depends on many factors, like rock type, degree of cementation, porosity, and depth of burial [49]. From experimental work (e.g., [16,19,49,52]), it appears that both the bulk rock and pore volume compressibility strongly depend on porosity. Several equations are formulated that relate the rock compressibility or the pore volume compressibility to porosity, e.g., [52–54]. However, the different studies result in different equations and it is beyond the scope of this work to thoroughly analyse the relation between porosity and rock compressibility.

5 Seismic Hazard Analysis

In Chapter 2 and 3, compaction creep in sands an possible mitigation options were investigated. The experiments suggested that the presence of AMP in the pore fluid inhibits compaction creep. Before an creep inhibiting agent can actually be introduced into a gas reservoir, it is important to understand if a small change in the rate of compaction creep can have a significant influence on the total compaction on the reservoir and associated induced seismicity and surface subsidence. This chapter and the next report about the preliminary study on the implementation of reservoir compaction in seismic hazard analyses and surface subsidence predictions. To ensure focus, the literature review only reports on results concerning the Groningen field.

5.1 Background

Seismicity is not unknown to the Groningen field. Since 1995, 240 earthquake events with a magnitude of a least 1.5 are recorded in the Groningen field, leading to numerous reports on damage to buildings [8,55]. These earthquake are related to depletion of the gas reservoir. Reduction of reservoir pressure induces reservoir compaction, which changes the poroelastic stress in and around the reservoir [56]. This can cause the stress acting on a pre-existing fault to increase and to equal the fault's resistance to slip, creating a critically stressed fault. Such a fault is prone to slip. Fault slip can be abrupt, which induces an earthquake, or it can occur by a stable creeping process, which does not induce an earthquake. Fault slip can also occur along fault subject to differential compaction, i.e. more compaction on one side of the fault relative to the other side.

In 2003, the *Mijnbouwwet* was implemented in the Netherlands, obliging operators to include a seismic hazard analysis in the production plans for oil and gas fields [21]. As a result, operators requested the research institutes TNO and KNMI to conduct a study on the hazard of induced seismicity. First reported in 2004 [57], the study was revised and updated in 2012 [58]. Within the study, TNO and KNMI performed a sub-study on seismic hazard by deterministic risk analysis [59,60] and probabilistic risk analysis [61–63], respectively. The NAM also performed a probabilistic risk analysis as part of the production plan for the Groningen field [8,64].

In short, a deterministic seismic hazard analysis is based on numerical simulation of earthquakes and their consequences. A probabilistic analysis is based on statistical methods to analyse past seismicity, which is used to construct probabilistic models to describe future seismicity. A more elaborate explanation is provides in the following sections, where first the deterministic seismic hazard analysis performed by TNO is described. Secondly, the probabilistic seismic hazard analyses performed by the KNMI and NAM are analysed. The purpose of this exploration is to determine how reservoir compaction is incorporated in seismic hazard analysis.

5.2 Deterministic Seismic Hazard Analysis

In a deterministic model, events (e.g., earthquakes) are completely determined by their causes and the outcome of the model is predetermined. All the data used in the model is known beforehand and the parameters have set values. Generally, the aim of a deterministic analysis is to define the limits for safe operation and to demonstrate that a site is tolerant to the identified hazard. Several advantages of a deterministic analysis are its transparency and the in- and output parameter are easy to understand [65]. However, uncertainty of the model and input data is not taken into account [65].

5.3 Deterministic Seismic Hazard Analysis by TNO

5.3.1 Method

TNO performed a deterministic seismic hazard analysis to calculate the seismic hazard induced in the onshore gas fields in the Netherlands [59,60]. Results from an original study in 2004 [57], indicate that there seems to be a correlation between parameters related to reservoir and production properties and the occurrence of induced seismicity in hydrocarbon fields. In order to identify the possible correlations between parameters and seismic activity, parameter values for each single field were plotted against the cumulatively released seismic energy. In the study of TNO [59,60], a correlation between parameters exists when there is a good distinguishing capacity, i.e., the points of the hydrocarbon fields with seismicity form relatively narrow clouds at relatively large parameter values (Figure 30). From 22 tested parameters, TNO found three that have a correlation with seismicity: pressure drop in the reservoir; fault density of the reservoir; and the stiffness ratio between seal and reservoir rock [59,60]. The compaction coefficient (described in Chapter 4) was also tested for correlation, but no significant correlation was found.

For the identified key parameters there is a threshold value below which seismicity is not observed. At parameter values above the threshold, there is a certain probability that seismicity occurs. This probability is determined by the amount of seismic active fields versus the non-seismic active fields. In the TNO study, the critical value for each key parameter was determined using Bayes' theorem. Bayes' theorem relates current probability to prior probability, refer to [59] for the derivation. The probability of seismicity in case the parameter values is larger than the critical value was computed using the Rule of Succession [59]. The Rule of Succession can be used in a situation where an experiment is repeated, which has two possible outcomes, either success or failure. If N experiments are conducted and R experiments result in success, then $N - R$ experiments result in failure. Under the condition that this observation is the only characteristic known of the experiment, then the probability that the next experiment will result in success equals

$$P(success) = \frac{R+1}{N+2}$$

Using the hypothesis that a producing gas field may or may not show induced seismicity and based on the observed seismicity in the past, the Rule of Succession can be used to define the probability that a gas field will show induced seismicity.

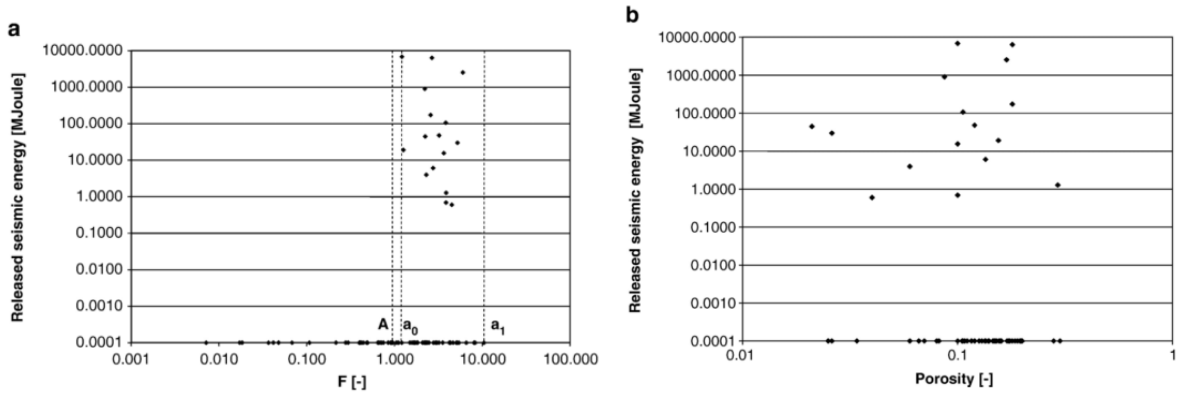

Figure 30: From [59]**. a) Example of parameter (fault density) with a good distinguishing capacity, b) example of parameter (porosity) with no distinguishing capacity.**

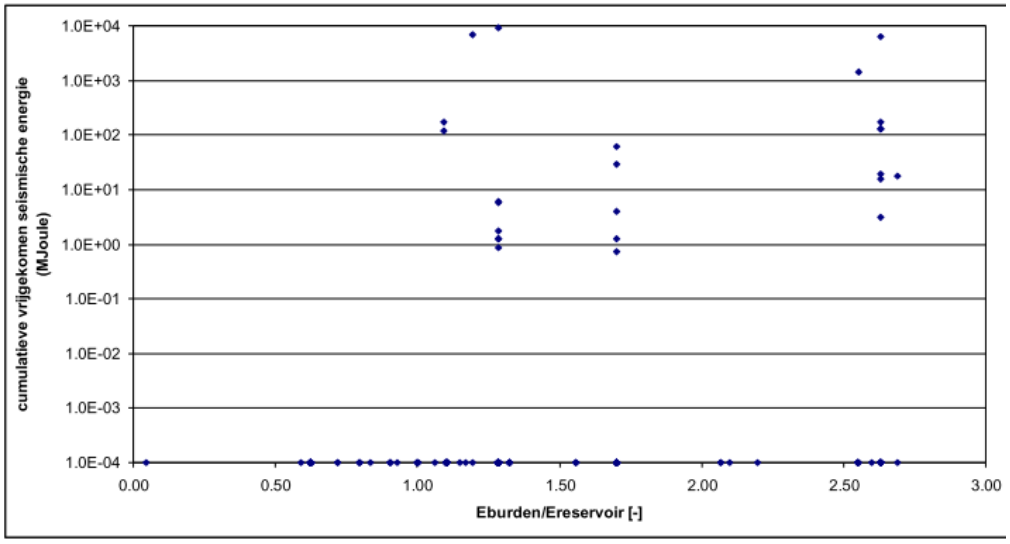

Figure 31: From [60]**. Cumulative released seismic energy versus the stiffness parameter.**

However, it must be noted that the probability of seismicity changes as more seismic events occur. As new seismic events are recorded the probabilities and critical vales must be updated. In addition, the probabilities and critical values can also change when more information about reservoir characteristics becomes available. In this work, only the critical values and probabilities of the most recent study by TNO [60] are presented.

5.3.2 Critical Values of Key Parameters

The first key parameter identified in the study of TNO was the pressure drop in the reservoir. The correlation is physically justified by the fact that a decrease in reservoir pressure as a result of depletion is the main driving force for stress disturbance and subsequent induced seismicity. In the 2012 study [60], the critical value for the relative pressure drop was determined at: $(\Delta P/P_{ini})_{critical} = 0.28 \pm 0.034$. Reservoirs with a relative pressure drop larger than 0.28 have a probability of induced seismicity, while reservoirs with a relative pressure drop smaller than 0.28 have a negligible probability.

The correlation of the second key parameter, fault density, can be physically explained by the fact that in the Netherlands hydrocarbon production-induced seismicity is mainly the result of the reactivation of existing faults [66]. For each gas field, fault density was calculated according to

$$F = \frac{fault\ area^{3/2}}{gross\ rock\ volume} = \frac{{l_b}^{3/2} \cdot h^{3/2}}{A \cdot h} = \frac{{l_b}^{3/2} \cdot \sqrt{h}}{A}$$

where l_b is the total fault length of all faults (boundary and intra-faults) mapped on top structure maps, A the surface area of the field and h the thickness of the reservoir. In the TNO study of 2012 [60], the critical value for the fault density was determined at: $F_{critical} = 0.86 \pm 0.29$. Reservoirs with a fault density larger than 0.86 have a probability of induced seismicity, while reservoirs with a fault density smaller than 0.86 have a negligible probability.

The third key parameter identified in the study of TNO was the stiffness parameter. The parameter was calculated for each field using the relation $S = E_{seal}/E_{reservoir}$, where E denotes the Young's modulus, which is a measure of the stiffness of an elastic material. The elastic

properties of the seal and the reservoir are important, because they affect the reactivation of faults. A relatively stiff seal promotes the reactivation of steeply dipping normal faults, which are not uncommon in the Dutch gas fields [66]. The critical value for the stiffness parameter was determined at $S_{critical} = 1.01 \pm 0.08$. Reservoirs with a stiffness parameter larger than 1.01 have a probability of induced seismicity, while reservoirs with a stiffness parameter smaller than 1.01 have negligible probability. In TNO's study, the parameter range above the critical value was further divided into two areas, because it was observed that the ratio between seismic and non-seismic fields increased with increasing stiffness parameter (Figure 31) [59,60]. Again following Bayes' theorem [59], a second boundary was defined at $S = 1.33$, creating two classes. For these classes, separate probabilities for seismicity were calculated.

5.3.3 Probability of Seismic Activity

In the study by TNO, some parameter conditions were identified for which there is a probability of seismic activity in an exploited field. The first condition is that there should be a significant pressure drop relative to the initial pressure ($\Delta P/P_{ini} \geq 0.28 \pm 0.034$). If this condition is not met, then there is no significant probability for seismicity, even though the other parameters are above the critical value. Secondly, in order to have the possibility of seismic activity both the fault density and stiffness parameter should exceed the critical value ($F \geq 0.86 \pm 0.29$ and $S \geq 1.01 \pm 0.08$).

In the study of 2012, this resulted in 84 reservoirs with favourable parameter conditions, of which actually 23 reservoirs experienced seismic activity [60]. Of the seismic active fields, 9 fields had a stiffness parameter in the lower range ($S \leq 1.33$), while the other fields had a stiffness parameter in the higher range ($S \geq 1.34$). Following the Rule of Succession, probabilities of seismic activity were calculated for the various classes, as presented in Table 6. In Figure 32, hazard maps are presented showing the calculated probability of seismic activity for fields located in the north of the Netherlands. The fields that already experienced induced seismic activity are indicated in red. From the hazard map (Figure 32), it appears that especially the fields located to the north east have a probability of seismicity, while the fields located to the south west have a negligible probability.

Table 6: Earthquake probabilities of the investigated fields after [60]

$\Delta P/P_{ini} \geq 0.28$	$F \geq 0.86$ and $S \geq 1.34$: $P = 0.42 \pm 0.08$
	$F \geq 0.86$ and $1.01 \leq S \leq 1.33$: $P = 0.19 \pm 0.05$
	$F < 0.86$ and/or $S < 1.01$: $P = 0$
$\Delta P/P_{ini} < 0.28$	$P = 0$

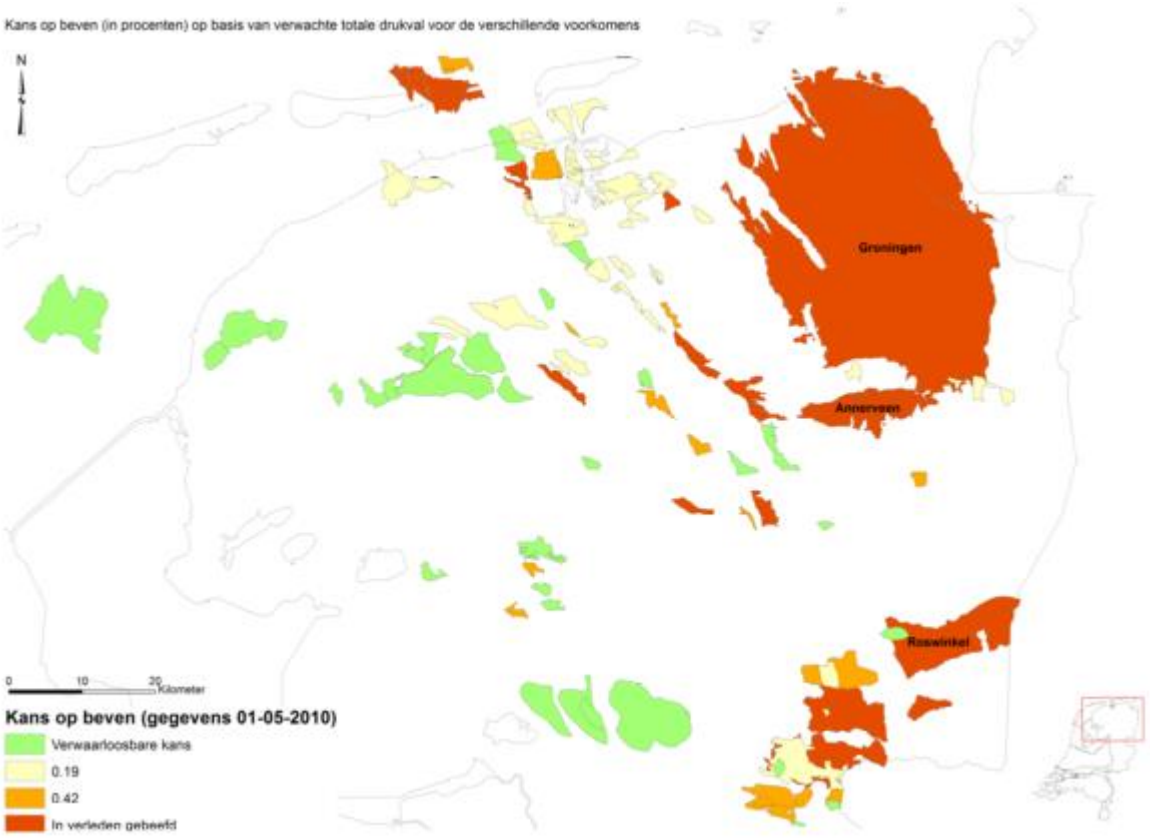

Figure 32: From [60]**. Probability of seismic activity based on the predicted pressure drop for the various fields in the north of the Netherlands.**

5.3.4 Discussion

In the TNO study [59,60], a correlation was found between three parameters related to reservoir and production properties and induced seismicity. For the three parameters (pressure drop, fault density and stiffness ratio) critical values were defined that marked the boundary of fields having either a probability for induced seismicity or a negligible probability. The compaction coefficient was also among the parameters tested for correlation. However, in TNO's study, no significant correlation was found between the compaction coefficient and induced seismicity.

The stiffness parameter defined in the TNO study depends on the Young's modulus of the seal and the reservoir. For a homogeneous isotropic material the Young's modulus can be related to the bulk rock compressibility (i.e., compaction coefficient). It must be realized that the bulk rock compressibility is the inverse of the bulk modulus ($K = 1/C_{bc}$), which is the resistance of a material to uniform compression. The bulk modulus and Young's modulus are related according to $E = 3K(1 - 2\nu)$, where ν is the Poisson's ratio, which is the ratio of lateral strain to longitudinal strain in an elastic body due to uniaxial longitudinal stress. Similar relations hold for poroelastic material [51] and combining them results in a Young' modulus that depends on the bulk compressibility according to

$$E = \frac{3}{C_{bc}}(1 - 2\nu)$$

Though in TNO's study no direct correlation was found between the compressibility coefficient and induced seismicity, the above relation shows that there is a dependency via the Young's

modulus. This mean that changing the rock compressibility will alter the Young's modulus of the reservoir, which will affect the probability of induced seismicity of that reservoir.

5.4 Probabilistic Seismic Hazard Analysis

In a probabilistic model, events can be identified by their probability of occurrence. Unlike a deterministic model, the outcome is not predetermined and the parameter values are selected from probabilistic distributions. These distributions can have various shapes, for example normal, lognormal, uniform or triangular. The shape of the distribution is a measure of the uncertainty of the data. Generally, the aim of a probabilistic analysis is to provide an estimate of the risk present at a site. Several advantages of a probabilistic analysis are the incorporation of uncertainty and the analysis reflects the actual knowledge of seismicity [65]. However, a probabilistic analysis is difficult to explain to a non-specialist and it is difficult to evaluate how a given input parameter affects the final result [65]. It should also be noted that probabilistic seismic hazard analysis can be only performed on fields that have experienced (induced) seismic activity, because the observed seismicity is used to model future seismicity.

5.4.1 Definition of Seismic Hazard

In both the KNMI [61–63] and the NAM study [8,64], seismic hazard is defined as the probability that a ground motion at a specific location will be exceeded during a time-period (i.e., return period). Earthquake ground motion is used instead of earthquake magnitude (i.e., the amount of energy released), because the nature of ground motion is more relevant to the potential impact of an earthquake on the built environment than earthquake magnitude.

This definition of seismic hazard is also used in the Eurocode 8; one of the technical standards for structural design set by the European Committee for Standardisation. Eurocode 8 specifically deals with the earthquake-resistant design of structures and sets a no-collapse requirement in order to protect life during and after a seismic event [67]. In this code, seismic hazard is presented as the probability that ground motion will be exceeded with a return period of 475 years, which is based on the haphazardly behaviour of natural earthquakes. However, the earthquakes observed in the Groningen field are the result of induced seismicity and for induced seismicity such a large return period is unlikely for two reasons. Firstly, in the seismic hazard analysis it is assumed there is no time delay between reservoir compaction and any associated induced seismicity. Secondly, the gas production lasts only a few decades, i.e., the duration of gas production is much shorter than the return period of 475 years. As an alternative interpretation, both KNMI and NAM used with smaller return periods, varying from one to ten years, which can model the hazard of induced seismicity more accurately.

5.5 Probabilistic Hazard Analysis by KNMI

5.5.1 Method

The KNMI conducted a probabilistic hazard analysis for several gas fields in the north of the Netherlands. Such an analysis consists of multiple components. The main components of KNMI's seismic hazard analysis are: the location of the earthquake with respect to the site (event location), the frequency and magnitude of the earthquake events (seismicity), the ground motions an event causes (ground motions) and the probability that a ground motion will be exceeded (hazard) [61]. These are explained accordingly.

Event location

In the KNMI study, it is assumed that seismicity is uniformly distributed over a defined seismic source area, located at an constant depth level of about 2.5 km. Furthermore, it is assumed that earthquakes behave as a Poisson process: they occur sequentially and independently from each other. As a result, the distance between source and site distribution function ($g(r)$) depends only on the site and source combination.

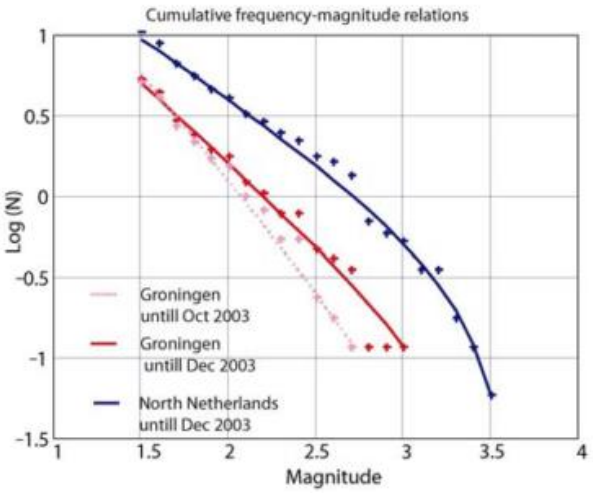

Figure 33: From [61]**. Annual cumulative frequency-magnitude relation for the all the field in the north of the Netherlands (blue), Groningen field until December 2003 (red) and Groningen field until October 2003).**

Seismicity

In order to define the seismicity in an area, a frequency-magnitude distribution is required. Such a distribution is derived from the observed seismic activity in the area and can be represented by a Gutenberg-Richter distribution. The Gutenberg-Richter distribution relates earthquake magnitude (M) to the number of earthquakes ($N(M)$) in any given region of at least that magnitude. The distribution is be described by the equation $\log N(M) = a - bM$, where a and b are constants. The b-value is characteristic for the seismicity in an area.

In the KNMI study, the constants of the Gutenberg-Richter relation were modified to fit the distribution to the seismicity observed in the period 1986-2003. In addition, the distribution was truncated at M_0 and M_{max}, which are the minimum magnitude relevant for hazard estimation and maximum magnitude assumed to occur, respectively. There are various statistical and physical methods to estimate the maximum magnitude, which are explained in detail in the KNMI studies [61,63]. The minimum and maximum magnitude used in the analysis are 1.5 and 3.5, respectively. Though higher maximum magnitude were determined, models with $M_{max} > 3.5$ had little influence on the resulting seismic hazard [61,62]. The alterations of the Gutenberg-Richter distribution result in a truncated normalized exponential cumulative frequency-magnitude distribution that has a good fit with the observed seismicity (Figure 33) [61]. For the Groningen field, the measured data up until October 2003 is described by $\log N = 2.7 - 1.3M$.

Ground motions

Ground motion prediction equations are empirical equations that can predict peak ground acceleration (PGA) and peak ground velocity (PGV) at any location. The equations depend any many factors, like focal mechanism, rupture process, site response and unknown details of the 3D structure. Selection of appropriate ground motion prediction equations for the Netherlands is difficult, because most equations are fit to ground motion data from large earthquakes ($M \geq 5$), while in the Netherlands earthquake magnitudes are much smaller (e.g. [68]).

In the KNMI study, the equations from [68] were adopted, because those equations appear to have a reasonable fit with the sparse ground motion data from the Netherlands [69]. In the KNMI study, it was recognized that the predicted PGA and PGV are uncertain. Consequently, the

PGA and PGV values are described by a lognormal distribution with a standard deviation. The standard deviation (σ) of the PGA varies in size depending of the size of the PGA. For PGA values lower than 0.068 g, $\sigma = 0.55$, and for PGA values exceeding 0.21 g, $\sigma = 0.39$ (g is the acceleration due to gravity). Between the specified PGA range, the standard deviation varies according to $\sigma = 0.173 - 0.140 \ln PGA$ [61]. The standard deviation for the PGV (σ_v) depends on the PGA's standard deviation according to $\sigma_v = \sqrt{\sigma^2 + 0.06^2}$ [61].

Hazard

The components described above can be combined into a probability equation. In the KNMI study, the probability that a ground motion a will be exceeded ($P[A > a]$) is expressed as

$$P[A > a] = \sum_{i=1}^{N} \lambda_i \int_0^{\infty} \int_{M_0}^{M_{max}} f_i(M) \cdot g_i(r) \cdot P(A > a|M, r)\, dM\, dr$$

where λ_i is a scaling factor representing the mean seismicity rate, which is assumed to be stationary and to equal the annual rate of occurrence of events with a magnitude above the set minimum magnitude ($M > M_0$); $f_i(M)$ is the frequency-magnitude distribution, describing the frequency of occurrence of events with magnitude M; $g_i(r)$ is a probability density function characterizing the probability that an event occurs at a distance r from the site; and $P(A > a|M, r)$ is the conditional probability function that for a given magnitude M and distance r the ground motion a will be exceeded. For one specific site the probability $P[A > a]$ can be obtained by summing the hazard due to all different seismic zones i.

5.5.2 Results

A selection of the results of KNMI's probabilistic seismic hazard analysis are presented in Figure 34 and Figure 35. The hazard maps constructed for the Groningen field (Figure 34) show that the hazard is uniformly distributed across the field and only at the edges of the field the hazard decreases. For the centre of the field there is a 10 % probability that the PGA will be exceeded at values between 200 and 225 cm/s^2 in one year or with PGA values between 225 and 250 cm/s^2 in ten years. From Figure 35, it can be observed that away from the fields the PGA values rapidly decrease. Overall, the Groningen field is expected to have higher PGA values than the Bergermeer and the Roswinkel fields.

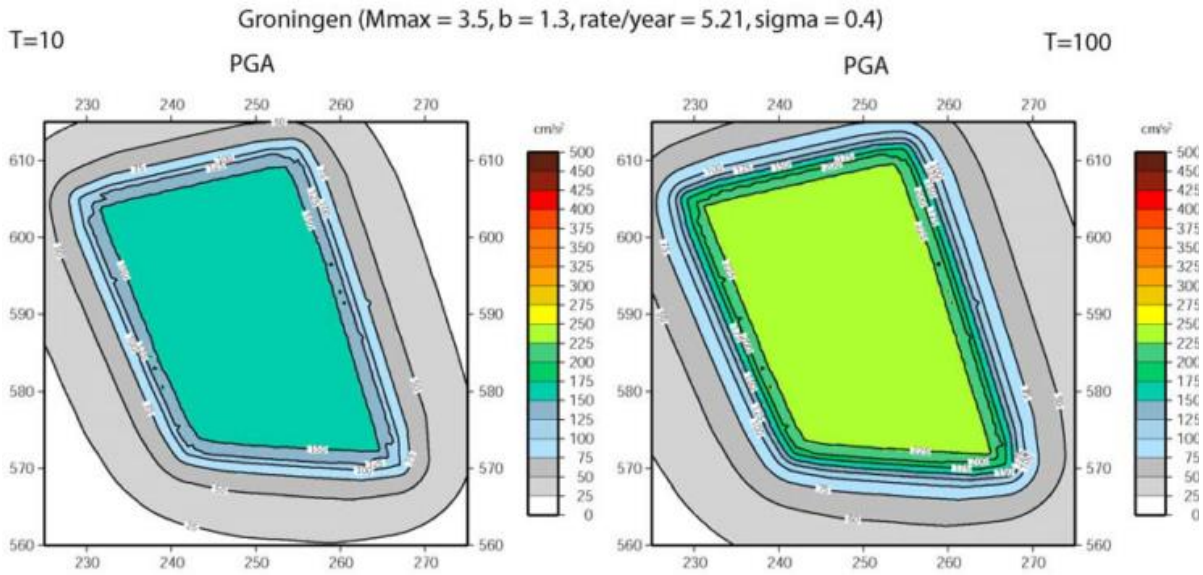

Figure 34: From [61]**. Estimated hazard at and around the Groningen field. The hazard maps indicate the potential hazard at each individual site on this maps. The hazard is presented at the PGA that may be exceeded once in T=10 years (left) and once in T=100 years (right). Alternatively, the hazard indicates a 10% probability that peak values as indicated can be exceeded within one year (T=10) or within ten years (T=100). The x- and y-axis indicate distance in kilometres.**

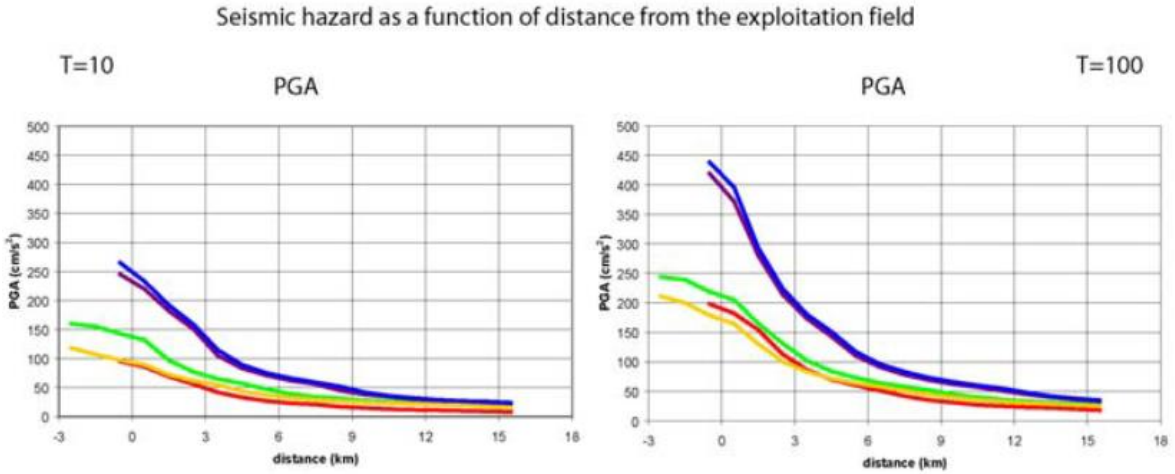

Figure 35: From [61]**. Seismic hazard as a function of distance from the surface projection of the exploitation field. Five examples are shown: the Groningen (green), the Bergermeer (purple), and the Roswinkel (blue) field and two hypothetical fields (yellow and red). PGA values are shown for two return periods, T=10 (left) and T=100 (right).**

5.5.3 Discussion

In the study by the KNMI [61–63], a probabilistic seismic hazard analysis is performed for the gas fields in the north of the Netherlands. The main components of the analysis are: earthquake location, seismicity, ground motion prediction and the prediction of the hazard. In the model, the causal relation between exploitation (rate) and seismicity is not fully incorporated [62]. A simple on/off model was assumed, with either exploration or no exploration and no pressure reduction dependency was incorporated. Furthermore, earthquake location was assumed to be completely random within the defined earthquake area, instead of being located near faults or areas of high compaction. Therefore, it appears that in the probabilistic analysis of the KNMI the effect of reservoir compaction on seismicity in not incorporated.

5.6 Probabilistic Hazard Analysis by NAM

NAM includes hazard analyses in the production plans for gas fields in the Netherlands. The hazard analyses used to be based on the results of the deterministic seismic hazard analysis by TNO as described in Section 5.2 (e.g. [70–72]). However, after the Huizinge earthquake (M 3.6) in August 2012, the NAM performed its own probabilistic seismic hazard analysis with a Monte Carlo approach for the Groningen field [8,64].

5.6.1 Method

The probabilistic seismic hazard analysis conducted by the NAM consists of similar components as the analysis performed by the KNMI. The main components of NAM's hazard analysis are: earthquake catalogue, event location, seismicity, ground motions and hazard [8]. These are explained in the following.

Earthquake catalogue

In NAM's hazard analysis, earthquake catalogues are defined in order to restrict the amount of seismic energy released during the life time of the Groningen field. For multiple catalogues, total seismic moment budgets were drawn from the total seismic moment budget distribution derived from the seismological model for the Groningen field (Figure 36). This seismological model is based on both a compaction model for the Groningen field and a statistical fault strain partitioning model. The fault strain partitioning model describes the fraction of reservoir volume change that is accommodated by seismogenic fault slip, i.e. fault slip accompanied by an earthquake [8].

Event location

In NAM's hazard analysis, locations of individual earthquake events are assigned by randomly sampling the expected event density map. This map is also derived from the Groningen compaction model, because there is a positive correlation between the amount of reservoir compaction and earthquake location [8]. Areas that experience more compaction have a higher event density compared to areas with less compaction.

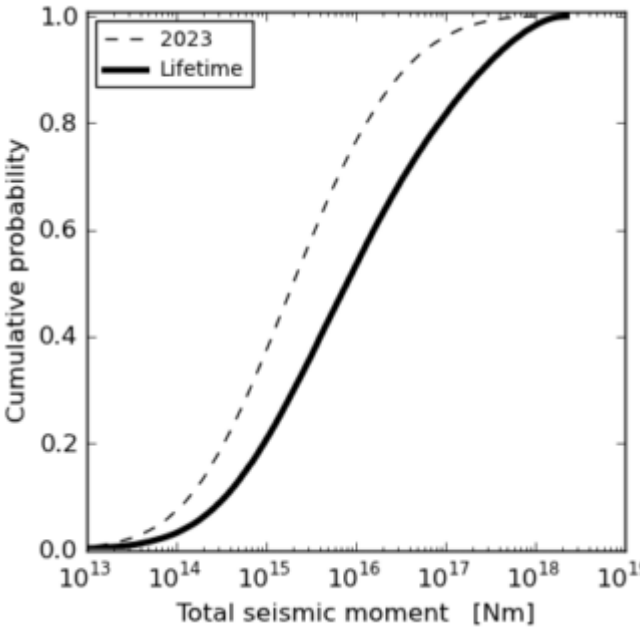

Figure 36: From [8]**. The cumulative probability distribution of total seismic moment, as predicted for the 10-year period 2013-2023 (dashed line) and for the remaining life time (solid line). Both are based on the current production plan and the time-decay compaction model.**

Seismicity

Magnitudes of individual earthquakes are appointed by randomly sampling a truncated Gutenberg-Richter distribution. Like the approach of the KNMI (Section 5.2.1), the NAM fitted the Gutenberg-Richter relation ($\log N(M) = a - bM$) to the observed seismicity in the period 1995 to 2012 (Figure 37) [8]. 1995 reflects the time when the monitoring network for detecting earthquakes of at least magnitude 1.5 was put in place [8]. The resulting distribution is truncated at

magnitudes 1.5 and 6.5. This specific range is selected, because magnitude 1.5 is the lower limit of the monitoring network that detects earthquakes in the Groningen field and magnitude 6.5 is the upper limit of earthquakes physically possible to be induced in the Groningen field, as calculated by the NAM [8]. In NAM's approach, sampling of the Gutenberg-Richter distribution is restricted in such a way that the sum of the seismic moments of individual earthquakes in a catalogue cannot exceed the seismic moment budget set for that catalogue (as described above).

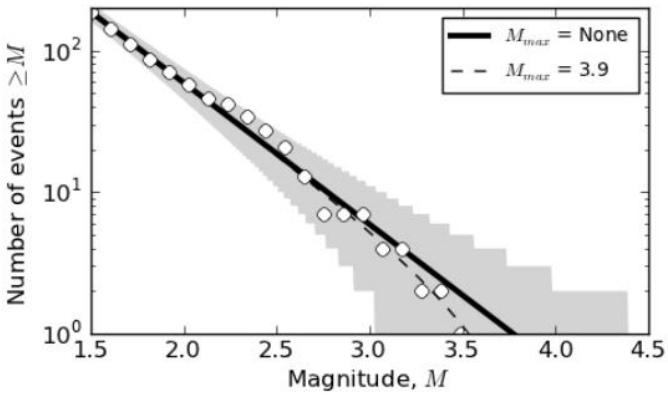

Figure 37: From [8]**. The cumulative frequency-magnitude distribution of earthquakes observed in the Groningen field. Circles denote the number of earthquakes of at least magnitude M. The black line is the frequency-magnitude model with b=1.0. The grey shading shows the 95% confidence interval associated with the model. The dashed line denotes an alternative frequency-magnitude model with also b=1.0, but zero probability of earthquakes above magnitude 3.9.**

Ground motions

For each seismic event, ground motions (PGA and PGV) are calculated at each node of the surface output grid. As described in the previous section (Section 5.2.1), ground motion prediction equations are empirically fitted equations. While KNMI used ground motion prediction equations from [68], the NAM applied the equations from [73]. The equations are modified to fit the ground-motion recording data from Groningen. Though there is a reasonable good fit (Figure 38), there is a scatter. As a result, the equations cannot predict unique PGA or PGV values for a given set of parameters. Instead, the equations give a probabilistic distribution of values of peak acceleration or velocity, which is randomly sampled around its mean to produce ground motions for each seismic event.

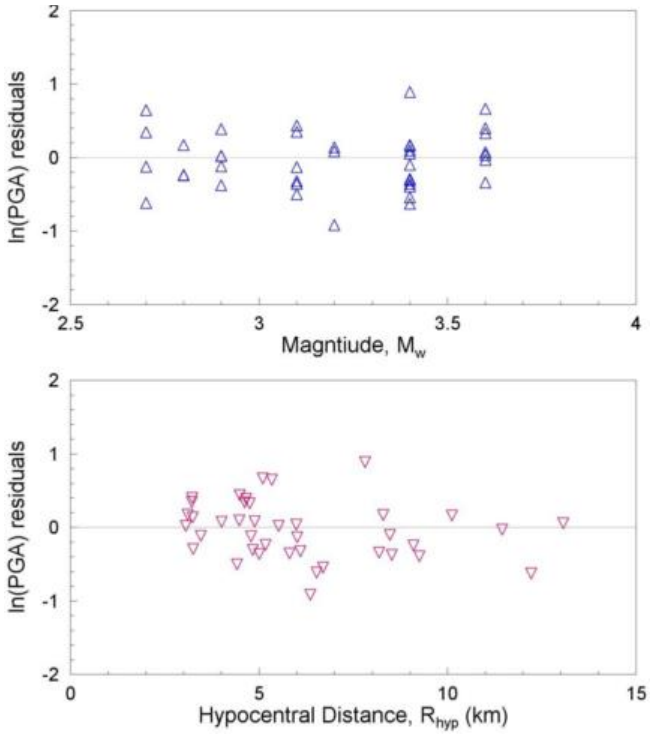

Figure 38: From [8]**. Residuals of PGA values calculated from the Groningen field with respect to the predictions from the adjusted equations from** [73]**. The residuals are calculated from the natural logarithm of the observed value minus the natural logarithm of the predicted median value.**

Hazard

The last step in the NAM's hazard analysis involves generating hazard curves for each surface location by counting the exceedances of specified ground motion thresholds and averaging over

the number of simulated catalogues. These curves can then be combined into hazard maps, showing where the ground motions exceed the set threshold and with what value.

5.6.2 Uncertainty Assessment by Logic-Tree

As part of the hazard analysis, the NAM assessed the influence of uncertainties on the outcome of the hazard analysis. The NAM especially focussed on epistemic uncertainties, which are uncertainties related to lack of (sufficient) knowledge. Based on experience of running the Monte Carlo hazard simulations and expert judgement, the NAM identified four key epistemic uncertainties: reservoir compaction, strain partitioning factor, Gutenberg-Richter b-value and GMPE. Other uncertainties were also considered, but regarded as negligible or beyond the scope of the work [8]. The impact of the identified uncertainties on the hazard assessment can be explored by employing a logic-tree analysis. The logic-tree is constructed based on the workflow of the seismic hazard assessment (Figure 39). The main branch of the logic tree represents the base case scenario (scenario 0). Each diverging branch is an alternative scenario where one parameter (i.e., key epistemic uncertainty) is varied with respect to the base case scenario. The result of the each alternative scenario hazard assessment can then be compared to the base case hazard assessment.

The results of the logic-tree analysis can be plotted in a tornado plot to compare variation in the maximum PGA with respect to the considered epistemic uncertainties (Figure 40). The greatest impact of those considered is imposed by the strain partitioning factor. Scaling of the GMPE and the choice of compaction model also have significant impacts, but much smaller compared to the strain partitioning factor. A negligible impact is observed for the b-value variations.

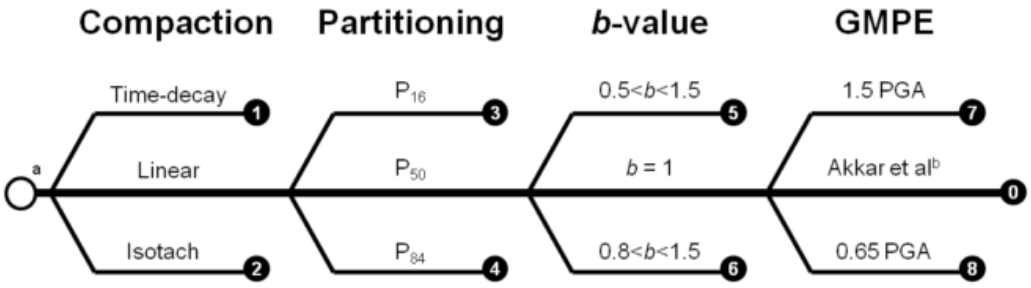

Figure 39: Logic-tree from [8]**. Numbers in black circles denote individual scenarios within the logic tree. Each scenario takes the base case scenario values (scenario 0) for all parameter with the exception of the parameter indicated by each branch of the logic-tree.**

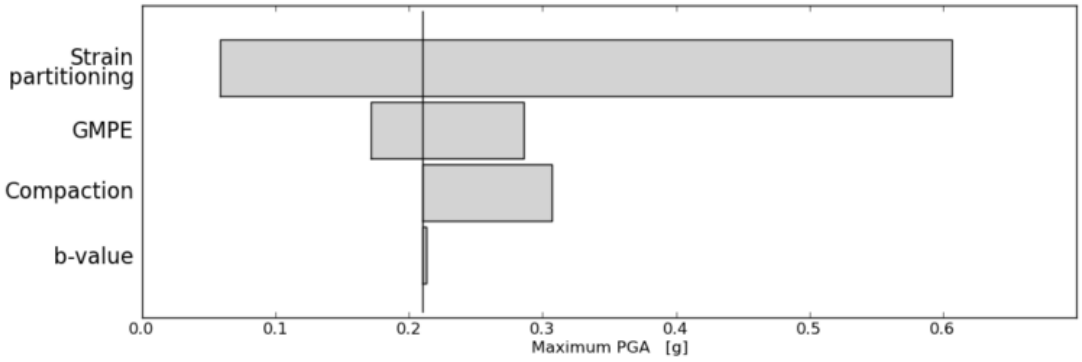

Figure 40: Tornado plot from [8]**. Variation in the maximum PGA found within the Groningen field with a 2% exceedance over the period 2013 to 2023 due to epistemic uncertainties represented in the logic-tree.**

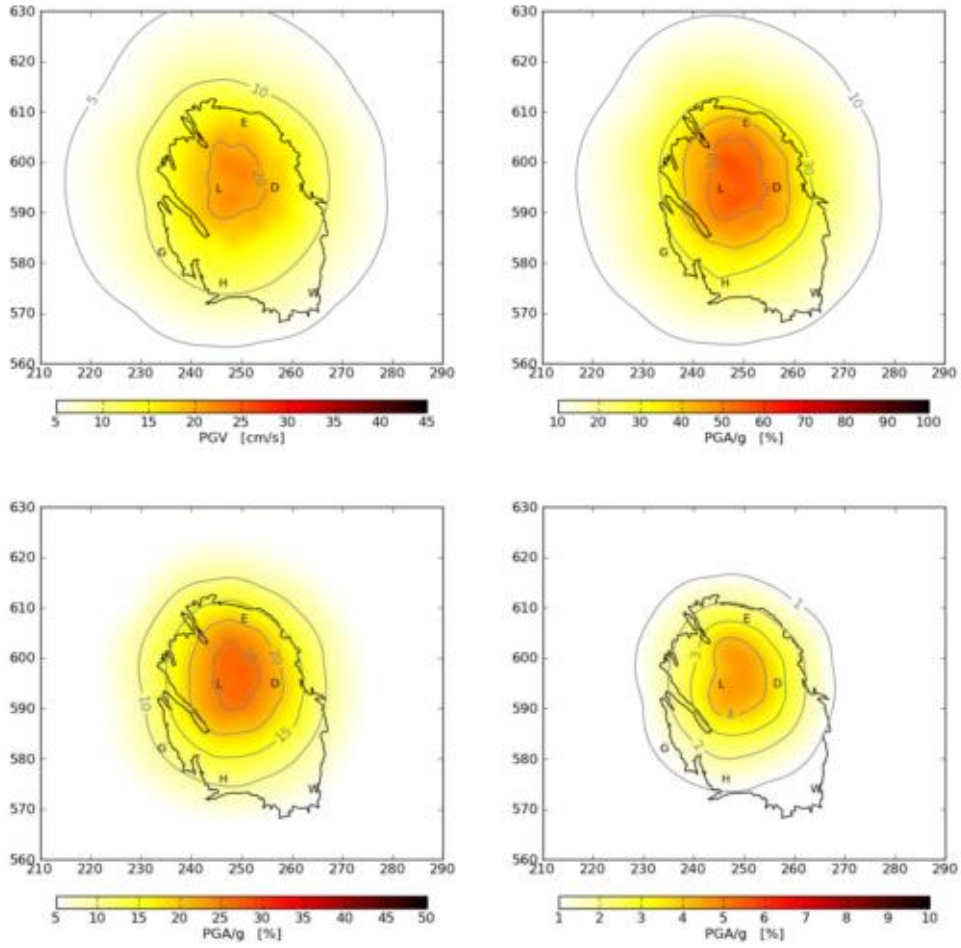

Figure 41: Hazard maps for the Groningen field from [8]**. Top row: predicted ground motion with an average annual 0.2 % chance of exceedance for the ten year interval of 2013 to 2023. The black line denotes the field outline and the letters D to W denote Delfzijl, Eemshaven, Groningen, Hoogezand, Loppersum and Winschoten, respectively. Bottom row: predicted ground motion with an average 10 % chance of exceedance and 50 % chance of exceedance for the ten year period of 2013 to 2023.**

5.6.3 Results

The results of the probabilistic seismic hazard analysis for the Groningen field by NAM are presented in the hazard maps of Figure 41. The maps show that the highest accelerations and velocities are expected in the centre of the field, where also the largest amount of compaction occurs [8]. In the ten year interval of 2013 to 2023, there is an average annual chance of 0.2 % that ground motions are exceeded with a maximum velocity of 22 cm/s and a maximum acceleration due to gravity of 57 %.

As part of the analysis, the NAM also tested the effect of various pressure depletion scenarios on the resulting hazard. Each pressure depletion scenario has five elements: a geological realisation, a compaction model, a development model, a production curtailment scenario and a production philosophy (Table 7). For each element there are several option, e.g., NAM tested four different compaction models. Out of the 288 possible permutations, NAM selected 19 scenarios for hazard analysis [8].

Table 7: From [8]**. Scenario elements considered by NAM for hazard analysis and the labels used to identify them.**

Label	Scenario Elements
	A. Geological Realisations
SubCor	Model realisation with Moderate NW aquifer
NoSubCor	Model realisation with Weak NW aquifer
	B. Reservoir Compaction Models
TD	Time decay
IT	Isotach
BL	Bi-linear
LN	Linear
	C. Development Scenarios
KHM1	KHM1 hook-up, 2nd and 3rd stage compression
NWP	D1 + North Western Periphery development
NWPSWP	D2 + South Western Periphery development
	D. Production Curtailment Scenarios
SN	Market Demand
C40	40 bcm/year
C30	30 bcm/year
C20	20 bcm/year
	E. Production Philosophies
Std	Current Production Philosophy
Tremor	Alternative Production Philosophy
Estop	Emergency stop

Figure 42 shows the results for various production scenarios, which NAM tested. Up until 2013, the different scenarios all show the same trend in reservoir volume change, annual volume change rate, seismic moment and seismic moment change rate, due to being fitted to historical data. After 2013, the scenarios generally display the same trend, except for the emergency stop scenario (red curve). In the emergency stop scenario, reservoir volume decreases to about $350 \cdot 10^6$ m^3 in 2035. After 2035, it stabilizes and some of the volume reduction is reversed. A similar trend is observed in the seismic moment: annual seismic moment increases up until to about 2020, after which it decreases. It must be noted that the results for the emergency stop

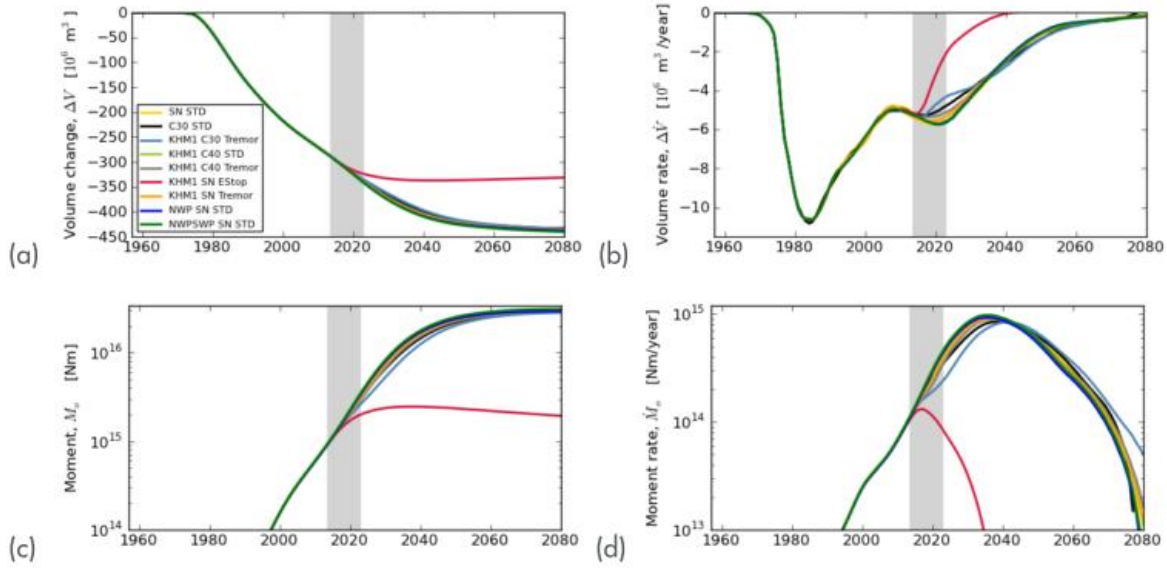

Figure 42: From [8]**. Comparison of the different production scenarios in combination with the time-decay compaction model according to (a,b) the cumulative and annual rates of bulk reservoir volume change and (c, d) the cumulative and annual rates of median seismic moment from 1960 to 2080.**

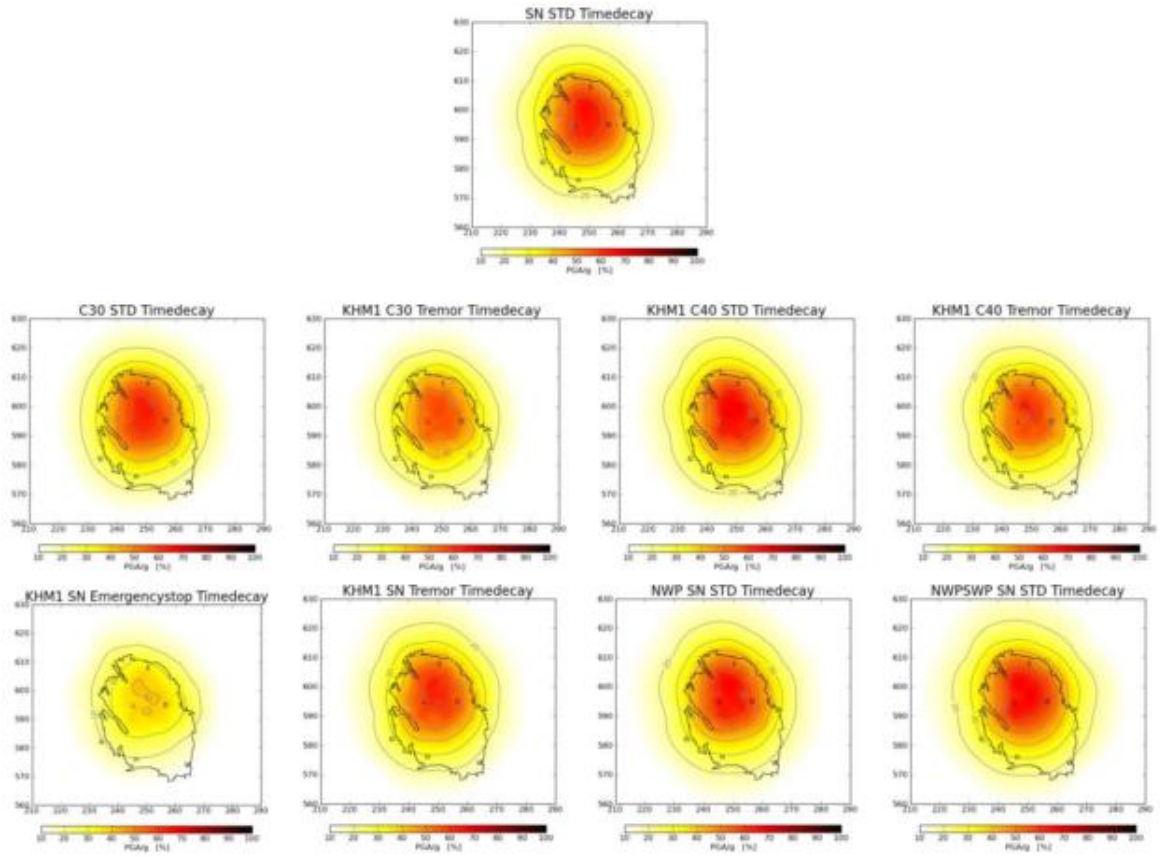

Figure 43: From [8]**. Influence of the different depletion scenarios on the PGA hazard. PGA hazard maps are shown for a 2% chance of exceedance over the period 2013 to 2023 based on the time-decay compaction model. The horizontal and vertical scales are the Rijksdriehoek coordinates in kilometre.**

scenario are applicable up to 2035, because the seismological model was developed for reservoir compaction and cannot model the reversal of compaction after 2035.

For the scenarios presented in Figure 42, NAM also constructed PGA hazard maps over the period of 2013 to 2023 (Figure 43). For most scenarios, the expected maximum PGA values with an exceedance probability of 2 % are similar and range from 0.64 g to 0.69 g (where g is the acceleration due to gravity taken to be 9.81 m/s^2). However, there are two exceptions (Figure 43), the emergency stop scenario and the KHM1 C30 Alternative (Tremor) scenario, which have a maximum PGA of 0.41 g and 0.58 g, respectively. In comparison to the SN STD scenario, this is an apparent hazard reduction of 38 % and 12 %, respectively.

5.6.4 Discussion

The NAM conducted a probabilistic seismic hazard analysis for the Groningen field. The analysis has a Monte Carlo approach and generates probabilities by sampling from various distributions. The main components are the event density map, determining earthquake location; a frequency-magnitude distribution for seismicity; a ground motion distribution; and hazard maps. Both the seismological model and the event density map are based on a compaction model. This indicates that reservoir compaction is thoroughly integrated in the analysis. The NAM tested various compaction models, which are analysed in the next chapter.

6 Compaction Models

In the hazard analysis, the NAM tested three compaction models: bi-linear, time-decay and isotach. The bi-linear was until 2011 the preferred model to model and predict reservoir compaction and surface subsidence. However, upon revision of the production plan for Ameland field, it appeared that the bi-linear model could not describe the ongoing surface subsidence above the field with reduced depletion rates [72]. In order to obtain better results, the NAM developed the new time-decay and isotach compaction model. The isotach compaction model overestimated the amount of reservoir compaction and surface subsidence, while the time-decay model produced a good fit with the observed subsidence. Consequently, the NAM selected the time-decay compaction model as the new base case model. In the following, the bi-linear and time-decay model are explained and predicted surface subsidence is presented.

6.1 Bi-Linear Compaction Model

The bi-linear compaction model from the NAM is based on the observed linear relation between strain and pore pressure in compaction experiments performed on Roltliegend sandstone cored from the Groningen field [8]. If the rock surrounding the reservoir also behaves in a linear manner, then a linear relation between pressure depletion in the reservoir and surface subsidence can be expected. Recalling Equation (4) from Chapter 4, the linear relation between pressure depletion and vertical strain, i.e. surface subsidence, is

$$e_z = c_m \Delta P \tag{5}$$

However, when plotting the measured surface subsidence against pressure depletion (Figure 44), a linear trend does not exist. Instead, the data is better approximated with two linear lines. The two lines describing reservoir compaction meet at a certain pressure, named the transition pressure. One line describes compaction before the transition pressure, while after the transition pressure compaction is described by the second line. The slope of the lines is equal to the uniaxial compaction coefficient. In NAM's analysis, the compaction coefficient is a function of porosity [8,74]. For the bi-linear compaction model, the compaction coefficient and porosity are linearly related according to

$$C_{mpre} = m_{pre}\varphi + c \tag{6}$$

$$C_{mpost} = m_{post}\varphi + c \tag{7}$$

where the subscript *pre* denotes prior to the transition pressure, *post* denotes after the transition pressure, and m and c are arbitrary parameters. The NAM determined the transition pressure and the parameters m and c by inversion, i.e., calibration of the subsidence model to the observed subsidence. Subsidence modelled for

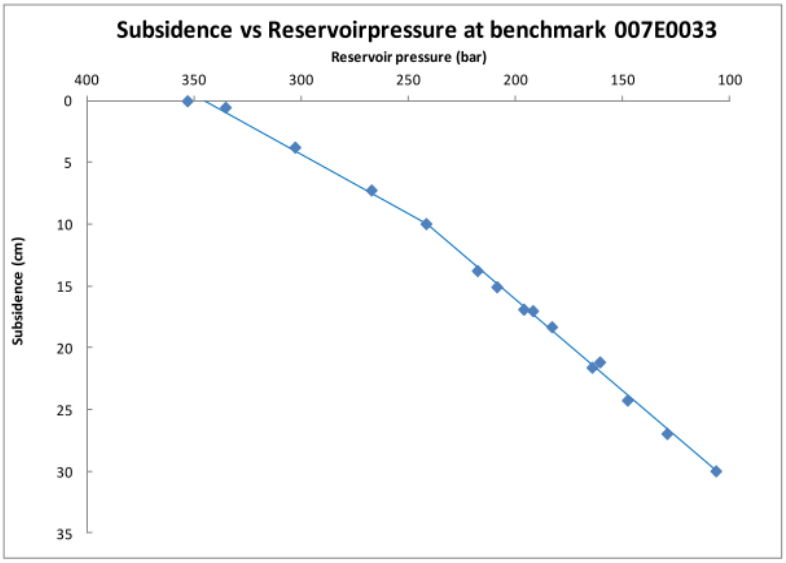

Figure 44: From [8]. Measured surface subsidence versus reservoir pressure (blue dots) at a benchmark in the Groningen field. The blue line illustrates the bi-linear trend in the data.

various time spans is compared to measured subsidence and residuals between the two are calculated. Next, the total variance weighted root-mean-square (RMS) value is calculated. The parameter combination resulting in the lowest RMS value is selected for modelling of future reservoir compaction and subsidence. The resulting parameters are

$$C_{mpre} = 1.31\varphi + 0.11$$

$$C_{mpost} = 3.14\varphi + 0.11 \tag{8}$$

$$P_{trans} = 234 \text{ bar}$$

Combining the resulting parameters with equations (6) and (7) gives

$$e_{zpre} = (1.31\varphi + 0.11)\Delta P$$

$$e_{zpost} = (3.14\varphi + 0.11)\Delta P \tag{9}$$

Equation is also used by NAM to model the future subsidence according to the bi-linear compaction model.

6.2 Time-Decay Compaction Model

The time-decay compaction model was developed by the NAM, because the bi-linear compaction model could not accurately model the ongoing subsidence above the Ameland field with reduced pressure depletion [8,72]. It was observed that surface subsidence is delayed and slowly accelerates with time. Instead of a linear relation, this suggests a time-decay relation between pressure reduction and subsidence. A possible cause for the time-delay is the effect of pressure diffusion, which is not yet properly modelled in the reservoir models. However, other time-dependent processes like salt creep of the salt layer above the reservoir or compaction creep of the reservoir, could also contribute to the time-decay relation. Without knowing the exact processes governing the time-delay, a time-decay function can formulated, because the resultant of a combination of independent time-decay processes is itself a time-decay process. The NAM proposed the following time-decay equation for surface subsidence, relating the constrained volume strain (e_{ii}) at a point (x) in the reservoir to the pressure change (ΔP) and the constrained uniaxial compressibility (c_m) convolved with a time decay function

$$e_{ii}(x,t) = \Delta P(x,t) c_m(x) *_t \frac{1}{\tau} \exp\left[\frac{-t}{\tau}\right] \tag{10}$$

where, t is time, $*_t$ is the convolution operator with respect to time, and τ is a time-decay constant.

In the NAM study, the best value for the time-decay constant was found by inversion using a semi-analytic geomechanical model. The approach to determine the best value is the same as described above for the bi-linear model. First, the residuals between the modelled and observed subsidence are calculated. Next, the RMS values are determined and the time-decay constant with the lowest RMS value is used in modelling of future compaction and surface subsidence. The time-decay constant is determined to be 7.3 years.

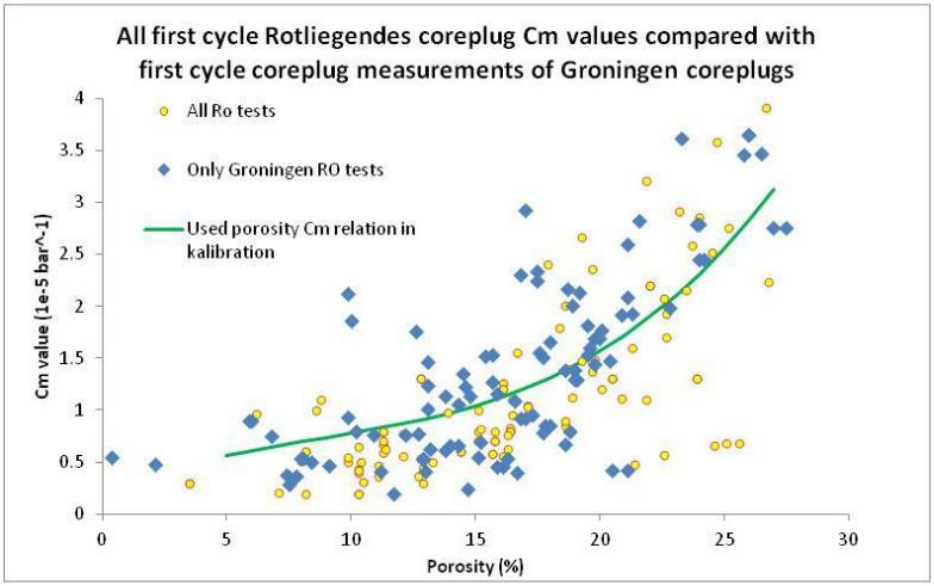

Figure 45: From [8]**. Experimental results for the uniaxial compaction coefficient versus atmospheric porosity for all sorts of Rotliegend sandstone (yellow circles) and for only Rotliegend sandstone from the Groningen field (blue diamonds). The green line denotes the porosity compaction coefficient relation used in calibration of the time-decay model.**

The uniaxial compaction coefficient is also partly determined using inversion by the NAM. Like in the bi-linear model, the compaction coefficient depends on porosity. However, for the time-decay model a different relation is used. In Figure 45, uniaxial compaction coefficients calculated from experiments performed on Rotliegend sandstone from the Groningen field and other locations are plotted against porosity. The NAM determined a trend line through this data, resulting in the following porosity compaction coefficient relation

$$c_m = 267.3\varphi^3 - 68.72\varphi^2 + 9.85\varphi + 0.21$$

where c_m is in 10^{-5} bar^{-1} and φ, denotes porosity. Modelling based on this compaction coefficient relation fitted the Ameland data subsidence data accurately [72]. However, in order to have a good fit with the Groningen subsidence data, a multiplication factor is needed

$$c_m = c_{mfactor}(267.3\varphi^3 - 68.72\varphi^2 + 9.85\varphi + 0.21) \quad (11)$$

This factor is also determined by the inversion procedure described above and resulted in a value of 0.45. Combining the values reported with Equation (10), the equation describing the time-decay compaction model becomes

$$e_{ii}(x,t) = \Delta p(x,t) \cdot 0.45(267.3\varphi^3 - 68.72\varphi^2 + 9.85\varphi + 0.21) *_t \frac{1}{7.3}\exp\left[\frac{-t}{7.3}\right]$$

This relation used by the NAM to model future subsidence according to the time-decay model.

6.3 Predicting Surface Subsidence

Forecasts for surface subsidence modelled by the NAM using the bi-linear and time-decay model are presented in Figure 46 and Figure 47, respectively. For both models the subsidence develops in a similar pattern, with the centre of the subsidence bowl in the north of the field. Between 2013 and 2018, the bi-linear model predicts slightly more subsidence than the time-decay model. However, for the period 2013-2018, the time-decay models more surface subsidence

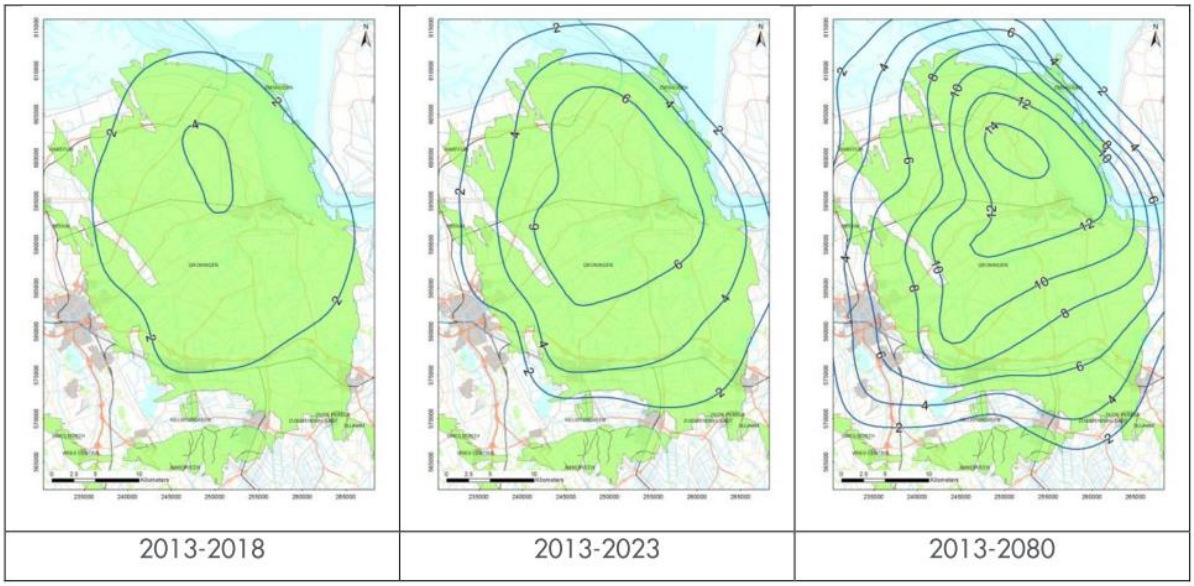

Figure 46: From [8]**. Subsidence forecast based on the bi-linear model for various time intervals [cm].**

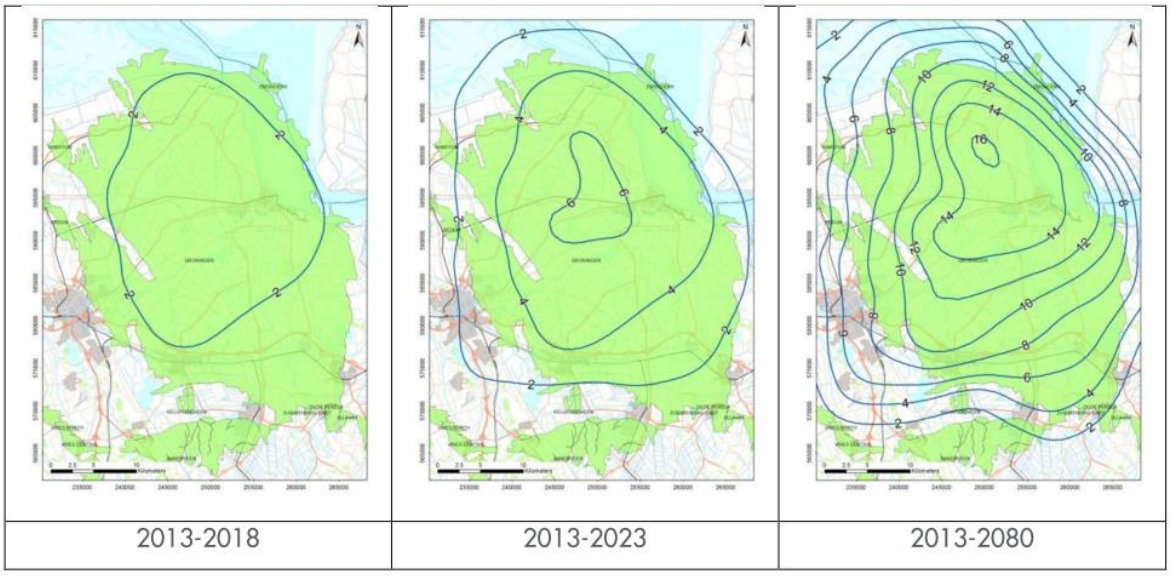

Figure 47: From [8]**. Subsidence forecast based on the time-decay model for various time intervals [cm].**

than the bi-linear model. This small relative increase in surface subsidence predicted by the time-decay model compared to the bi-linear mode, represents the subsidence delay nature of the model. The difference in predicted subsidence is very small. This may be related to the small difference in the compaction coefficients of the two models (Figure 48).

6.4 Discussion

The NAM tested a bi-linear compaction model and a time-decay compaction model. The bi-linear model is a simplistic representation of reservoir compaction and its effect on the surface. It assumes that both the reservoir and the surrounding rocks behave linearly. However, as noted in Chapter 4, the reservoir rock in the Groningen gas field is a porous rock and behaves in a poroelastic manner. In addition, the reservoir compaction is also the result of time-dependent creep, which is not a linear process. In this sense the time-decay compaction model is a better approximation of reservoir compaction. Though the model is not based on specific mechanisms

or processes, it does incorporated a time-dependent element. It is interesting to note, that though the two models vary greatly, they do results in more or less similar subsidence.

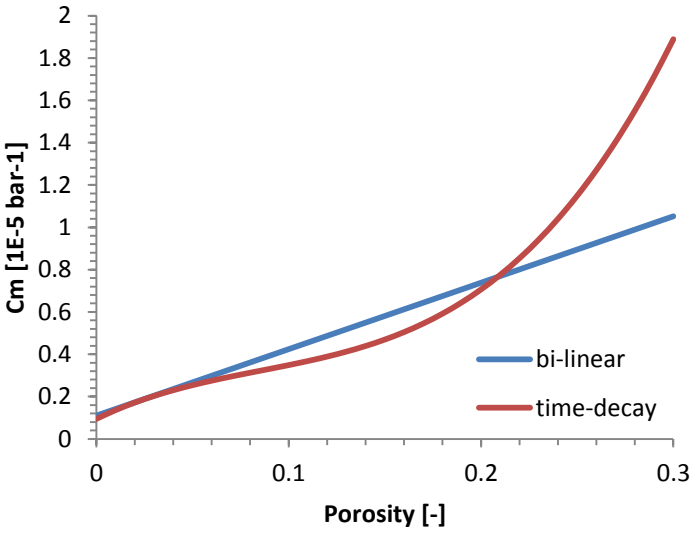

Figure 48: Compressibility coefficient as function of porosity for the bi-linear model (blue) and the time-decay model (red), calculated using Equation (8) and Equation (11) with a Cmfactor of 0.45, respectively.

7 Conclusion

The steel tube experiments suggested an inhibiting effect of the AMP solution on compaction creep. However, this effect could not be confidently verified, due to the poor reproducibility of the steel tube experiments. This was caused by one or multiple faulty elements in the methodology or set-up, like the extreme effect of opening and closing the temperature box or some influence of the Teflon liner. However, within the limits of this study it was impossible to pin-point the exact cause. It was therefore decided to try similar experiments in the Instron loading frame.

The inhibiting effect of AMP was initially not verified by the Instron experiments. It appeared that pre-compaction at 45 MPa created a locked sample, which could not be deformed during creep at 35 MPa. Therefore, instead of pre-compacting the samples, the samples were crushed to a set starting porosity. Yielding better results, it could be used to deduce that initial time-independent compaction of quartz sand is mainly controlled by grain rearrangement and grain scale microcracking. The subsequent time-dependent compaction (i.e. compaction creep) is controlled by subcritical microcracking. Both mechanisms are enhanced in the presence of water (i.e. stress corrosion cracking), due to the hydrolysis of weaker $Si-O$ bonds. Furthermore, it was found that the presence of AMP in the pore fluid inhibits compaction creep. It is interfered that the large AMP molecules block the entrance to the micro-cracks, inhibiting water to enter the crack. The water already present in the crack is consumed during microcracking, which eventually results in a relatively dry crack.

From the literature analysis, it appeared that reservoir compaction is integrated differently in each analysed method. In the TNO study on deterministic seismic hazard analysis, no direct correlation between reservoir compaction and seismicity was found. However, a correlation between the Young's modulus of the reservoir with respect to the Young's modulus of the seal and seismicity was found. The Young's modulus is an elastic parameter which can be related compressibility of the reservoir. This indicates an indirect relation between reservoir compaction and seismicity. In the KNMI study on probabilistic seismic hazard analysis, there was a minimal integration of reservoir compaction. In the model, production was either "on" or "off", and likewise compaction and seismicity were either "on" or "off". In the NAM probabilistic seismic hazard analysis, reservoir compaction was thoroughly integrated. Both the location of seismic events and the amount of seismic energy released were related to reservoir compaction via a compaction model. The NAM also predicted surface subsidence using different compaction models. The bi-linear and time-decay model were discussed and both predicted similar amounts of surface subsidence.

The fact that two different models predict similar surface subsidence is interesting. It raises the question if changing something relatively small, like the rate of compaction creep by adding a mitigation agent, still can have an effect on the rest of the system, like seismicity and surface subsidence, while two different models have similar predictions for subsidence. Therefore, more research is needed on the various parts of the system. The observed inhibiting effect of AMP needs to be thoroughly investigated by, for example, microstructural analysis. In addition, it is important to get a better understanding of the effect of changing small parameters on the outcome of a model.

Acknowledgements

Firstly, thanks to my supervisors Chris Spiers, Suzanne Hangx and Andrea Ramirez. Chris, thank you for providing me the opportunity to do this research and for your support and confidence. Suzanne, thank you for teaching me the secret workings of the lab and for your guidance in conducting experiments and writing. Andrea, thank you for introducing me to a new area of research and for your guidance on proceeding on the right track.

Secondly, thanks to the staff of the HPT-lab. A special thanks goes to Gert Kastelein, Eimert de Graaff and Peter van Krieken for their technical support and to Miao Zhang and Tim Wolterbeek for their help with the Instron machine.

Thirdly, a big shout out to Martijn van den Ende, Luuk Hunfeld, Evangelos Korkolis and Ronald Pijnenburg for always bringing a sparkle to my days at the lab.

Lastly, thanks to my friends and family. Thomas, thank you for your patience and never ending confidence.

Appendix A

This section describes the calculation to obtain intergranular pressure solution strain rates as mentioned in Section 3.3.3.1. The approach is similar to the approach of [10] and is based on the pressure solution model of [39]. The pressure solution model assumes a stressed granular aggregate made of spherical grains, containing fluid in the pores and in the grain boundaries. In such a system, differences in normal stress exist between the stressed grain contacts and the unstressed pore walls. This induces gradients in chemical potential of the solid and hence gradients in solubility of the solid [35,39]. The difference in chemical potential ($\Delta\mu_n$) between the grain boundary and grain pores is the thermodynamic driving force for transport and can be defined as

$$\Delta\mu_n = \mu_{gb} - \mu_p = (\sigma_n - P_p)\Omega^s \tag{A1}$$

where μ_{gb} denotes the chemical potential of the grain boundary, μ_p is the chemical potential of the pore wall, σ_n is the compressive normal stress acting on the grain contacts [Pa], P_p is the pore fluid pressure [Pa], and Ω^s is the molar volume of the solid [m^3/mol].

The difference in chemical potential is accompanied by a difference in solubility between the grain contacts and the pore walls. Due to the stress at the grain contact, the solid at the grain contact dissolves more easily compared to the solid at the pore walls. As a result, the grain contacts and pore walls act as sources and sinks, respectively. The difference in chemical potential is related to the enhanced solubility according to the relation

$$\Delta\mu_n = RT \ln\left(\frac{C_p + \Delta C}{C_p}\right) \approx RT\left(\frac{\Delta C}{C_0}\right) \tag{A2}$$

where R is the universal gas constant [J/mol K], T is the absolute temperature [K], C_p is the solubility of the solid at the sink [m^3/m^3], ΔC is the enhanced solubility at the pore walls, and C_0 is the solubility of the solid grains under purely hydrostatic conditions [m^3/m^3]. Generally C_p is almost equal to C_0.

At the stressed grain contacts, the solid dissolves, subsequently the solid diffuses via the pore fluid to the pore walls where it precipitates. These three steps are serial processes, of which is the slowest is rate controlling [22,39]. Assuming dissolution is the rate controlling process, equation (A1) can be inserted into a linear kinetic law describing grain boundary dissolution [39], to obtain an equation for strain rate ($\dot{\varepsilon}_s$) as a result of dissolution controlled pressure solution

$$\dot{\varepsilon}_s = A_s \frac{I_s(\sigma_n - P_p)\Omega^s}{dRT} f_s(\varphi) \tag{A3}$$

where A_s is a geometrical constant, I_s is the reaction rate coefficient for dissolution at the grain contacts [m/s] – defined as $I_s = k_s\Omega^s$, where k_s is the standard geochemical dissolution rate coefficient [mol/m^2 s] – d is the initial grain size [m], and $f_s(\varphi)$ is a dimensionless function of porosity (φ), which for a granular aggregate with a porosity of 5-40 % can be written as $f_s(\varphi) \approx 1/(1-2\varphi)$ [39].

Using equation (A3) and the dissolution rate data for quartz [75], the strain rate generated by dissolution-controlled pressure solution is calculated. Using the data in Table A1, the resulting prediction for strain rate is in the order of 10^{-14} s^{-1}. The assumption that dissolution is the rate controlling process, is justified by the fact that at high porosities (like the porosities used in this study), the area of dissolving grain contact is generally much smaller than pore wall area where precipitation occurs [39]. Since a smaller reaction area results in a slower process, dissolution is most likely slower than precipitation and consequently rate controlling. Furthermore, diffusion is most likely not rate controlling, because in silicate minerals diffusion-controlled pressure solution is generally faster than reaction-controlled (i.e. dissolution and precipitation) mechanisms [39]. In addition, the pore fluids used in this study are either lab air or silica saturated solutions. Dissolution of silica in a silica saturated solution is very slow, suggesting that dissolution is the rate-controlling process. However, if it appears either diffusion or precipitation is rate-controlling (i.e. the slowest process), the predicted strain rate is an upper bound value.

The above equations can also be used to determine the strain rate generated by simple dissolution of the solid in an undersaturated pore fluid. When the initial solution is completely undersaturated (solute free) and no stress is applied, $\Delta C = C_0$ in equation (A2), so that $\Delta\mu_n = RT$. Combining this with equation (A3) and using the data in Table A1, yields a strain rate due to dissolution in the order of 10^{-14} s^{-1}.

Table A1: Input Parameters Strain Rate Calculation

Parameter	Value	Unit
k_s [a]	3.6 x 10^{-13}	mol/m^2 s
Ω^s	2.3 x 10^{-5}	m^3/mol
σ_n	35	MPa
P_p	0	MPa
d	250	µm
R	8.31	J/mol K
T	298.15	K
φ	35.5	%

[a] dissolution rate data from [75].

References

[1] Eurostat. Energy, transport and environment indicators. 2013.
[2] IEA. World Energy Outlook 2013-Factsheet. 2013.
[3] Economic and Finanical Affairs European Commission. European Economy Member States' Energy Dependence: An Indicator-Based Assessment. 2013.
[4] GEA. Global Energy Assessment-Towards a Sustainable Future. 2012.
[5] ECF. Power Perspectives 2030-On the road to a decarbonised power sector. 2011.
[6] Doornhof D, Kristiansen TG, Nagel NB, Pattillo PD, Sayers C. Compaction and Subsidence. Oilf Rev 2006;18:50–68.
[7] TNO. Toetsing van de bodemdalingsprognose en seismische hazard ten gevolge van gaswinning van het Groningen veld. 2013.
[8] NAM. Technical Addendum to the Winningsplan Groningen 2013-Subsidence, Induced Earthquakes and Seismic Hazard Analysis in the Groningen Field. 2013.
[9] Minister van Economische Zaken. TK 2012-2013 33529 no.2-Gaswinning Groningen-veld. 2013.
[10] Hangx SJT, Spiers CJ, Peach CJ. Creep of simulated reservoir sands and coupled chemical-mechanical effects of CO2 injection. J Geophys Res 2010;115.
[11] Hangx S, Linden van der A, Marcelis F, Bauer A. The effect of CO2 on the mechanical properties of the Captain Sandstone: Geological storage of CO2 at the Goldeneye field (UK). Int J Greenh Gas Control 2013;19:609–19.
[12] Brzesowsky RH. Micromechanics of Sand Grain Failure and Sand Compaction. Utrecht University, 1995.
[13] Hollebeek E. The effect of fluid additives on the compaction creep of sand aggregates and sandstones cylinders 2012.
[14] Chester FM, Chester JS, Kronenberg AK, Hajash A. Subcritical creep compaction of quartz sand at diagenetic conditions: Effects of water and grain size. J Geophys Res 2007;112.
[15] Brantut N, Heap MJ, Meredith PG, Baud P. Time-dependent cracking and brittle creep in crustal rocks: A review. J Struct Geol 2013;52:17–43.
[16] Schutjens P, Heidug W. On the pore volume compressibility and its application as a petrophysical parameter. 9th Bienn Int Conf Expo Pet Geophys 2012:17.
[17] Teeuw D. Prediction of Formation Compaction from Laboratory Compressibility Data. Soc Pet Eng J 1971;251:263–71.
[18] Rhett DW, Teufel LW. Effect of Reservoir Stress Path on Compressibility and Permeability of Sandstones. Proc SPE Annu Tech Conf Exhib 1992:965–72.
[19] Oliveira de GLP, Ceia de MAR, Misságia RM. Experimental measurements of pore volume compressibility of sandstones and carbonates. 13th Int Congr Barzillian Geophys Soc 2013:6.
[20] Hamilton J, Shafer J. Measurement of pore compressibility characteristics in rock exhibiting pore collapse and volumetric creep. SCA Conf Pap 1991;9124:14.
[21] Staatssecretaris van Economische Zaken. Besluit van 6 december 2002, houdende regels ter uitvoering van de Mijnbouwwet (Mijnbouwbesluit). Staatsbl van Het Koninkr Der Ned 2002;604:123.
[22] Meer De S, Spiers CJ. Uniaxial compaction creep of wet gypsym aggregates. J Geophys Res 1997;102:875–91.
[23] Visser HJM, Spiers CJ, Hangx SJT. Effects of interfacial energy on compaction creep by intergranular pressure solution: Theory versus experiments on a rock analog (NaNO3). J Geophys Res 2012;117.
[24] Zhang X, Spiers CJ. Compaction of granular calcite by pressure solution at room temperature and effects of pore fluid chemistry. Int J Rock Mech Min Sci 2005;42:950–60.
[25] Iler. Chemistry of Silica: solubility, polmerization, colloid and surface properties, and biochemistry. 1978.
[26] Rimstidt JD. Quartz solubility at low temperatures. Geochim Cosmochim Acta 1997;61:2553–8.

[27] Morey GW, Fournier RO, Rowe JJ. The solubility of quartz in water in the temperature interval from 25 °C to 3OO°C. Geochim Cosmochim Acta 1962;26:1029–43.
[28] Pluymakers A, Peach CJ, Spiers CJ. Journal of Geophysical Research : Solid Earth anhydrite fault gouge under static conditions. J Geophys Res Solid Earth 2014;119:1–26.
[29] Demadis KD, Katarachia SD. Metal-Phosphonate Chemistry: Synthesis, Crystal Structure of Calcium-Amino Tris -(Methylene Phosphonate) and Inhibition of Caco 3 Crystal Growth. Phosphorus Sulfur Silicon Relat Elem 2004;179:627–48.
[30] Liddell RW. Methods and Compositions for Inhibiting Scale in Saline Water Evaporators. US Pat Off 1970;CIII-PXOM:7.
[31] Demadis KD. Chemistry of Organophosphonate Scale Inhibitors, Part 4: Stability of Amino-tris-(Methylene Phosphonate) Towards Degradation by Oxidizing Biocides. Phosphorus Sulfur Silicon Relat Elem 2006;181:167–76.
[32] AkzoNobel. AkzoNobel mTA-Salt Safe savings - the future of chlorine electrolysis n.d.:3.
[33] AkzoNobel. AkzoNobel mTA: The green alternative for anti-caking in road salt 2010:4.
[34] Brzesowsky RH, Spiers CJ, Peach CJ, Hangx SJT. Time-independent compaction behavior of quartz sands. J Geophys Res Solid Earth 2014;199:21.
[35] Niemeijer A., Spiers C., Bos B. Compaction creep of quartz sand at 400–600°C: experimental evidence for dissolution-controlled pressure solution. Earth Planet Sci Lett 2002;195:261–75.
[36] Noort van R, Spiers CJ, Pennock GM. Compaction of granular quartz under hydrothermal conditions: Controlling mechanisms and grain boundary processes. J Geophys Res 2008;113.
[37] Schutjens PMTM. Experimental compaction of quartz sand at low effective stress and temperature conditions. J Geol Soc London 1991;148:527–39.
[38] Chester J., Lenz S., Chester F., Lang R. Mechanisms of compaction of quartz sand at diagenetic conditions. Earth Planet Sci Lett 2004;220:435–51.
[39] Spiers CJ, Meer De S, Niemeijer AR, Zhang X. Kinetics of rock deformation by pressure solution and the role of thin aqueous films. In: Nakashima S, Spiers CJ, Mercury L, Fenter PA, Hochella MFJ, editors. Physicochem. Water Geol. Biol. Syst., Tokyo, Japan: Universal Academy Press, Inc.; 2004, p. 129–58.
[40] Griffith AA. The Phenomena of Rupture and Flow in Solids. Philos Trans R Soc London 1921;221:163–98.
[41] Zhang J, Wong T-F, Davis DM. Micromechanics of pressure-induced grain crushing in porous rocks. J Geophys Res 1990;95:341.
[42] Hertz H. Über die Berührung fester elastischer Körper. J Für Die Reine Und Angew Math 1881;92:156–71.
[43] Shah KR, Wong T-F. Fracturing at contact surfaces subjected to normal and tangential loads. Int J Rock Mech Min Sci 1997;34:727–39.
[44] Atkinson BK. A Fracture Mechanics Study of Subcritical Tensile Cracking of Quartz in Wet Environments. Pageoph 1979;117:1011–24.
[45] Atkinson BK, Meredith PG. Letter Section Stress corrosion cracking of quartz: a note on the influence of chemical environment. Tectonophysics 1981;77:T1–11.
[46] Dove PM. Geochemical controls on the kinetics of quartz fracture stresses 1995;100:22349–59.
[47] Atkinson BK. Subcritical crack growth in geological materials. J Geophys Res 1984;89:4077–114.
[48] Gill JS, Varsanik RG. Computer Modeling of the Specific Matching Between Scale Inhibitors and Crystal Structure of Scale Forming Minerals. J Cryst Growth 1986;76:57–62.
[49] Geertsma J. Land Subsidence Above Compacting Oil and Gas Reservoirs. J Pet Technol 1973;25:734–44.
[50] Holt RM, Brignoli M, Kenter CJ. Core damage effects on compaction behaviour. Soc Pet Eng 1994:55–62.
[51] Jaeger J., Cook NGW, Zimmerman RW. Fundamentals of Rock mechanics. 2007.

[52] Chuanliang L, Xiaofan C, Zhimin D. A New Relationship of Rock Compressibility with Porosity. Proc SPE Asia Pacific Oil Gas Conf Exhib 2004;SPE 88464:5.
[53] Schutjens PMTM, Hanssen TH, Hettema MHH, Merour J, Bree de P, Coremans JWA, et al. Compaction-Induced Porosity/Permeability Reduction in Sandstone Reservoirs: Data and Model for Elasticity-Dominated Deformation. SPE Reserv Eval Eng 2004:202–16.
[54] Hall HN. Compressibility of Reservoir Rocks. Pet Trans AIME 1953;198:309–11.
[55] NAM. http://feitenencijfers.namplatform.nl/aardbevingen/ 2015.
[56] Segall P. Geology Earthquakes triggered by fluid extraction Earthquakes triggered by fluid extraction. Geology 1989;17:942–6.
[57] Wassing BB. (TNO), Eck van T (KNMI), Eijs van RMHE (TNO). Seismisch hazard van geïnduceerde aardbevingen Integratie van deelstudies. vol. NITG 04-24. 2004.
[58] Wassing BB. (TNO), Dost B (KNMI). Seismisch hazard van geïnduceerde aardbevingen-Integratie van deelstudies. 2012.
[59] Eijs van RMHE, Mulders FMM, Nepveu M, Kenter CJ, Scheffers BC. Correlation between hydrocarbon reservoir properties and induced seismicity in the Netherlands. Eng Geol 2006;84:99–111.
[60] Thienen-Visser van K, Nepveu M, Hettelaar J. Deterministische hazard analyse voor geïnduceerde seismiciteit in Nederland. 2012.
[61] Eck van T, Goutbeek F, Haak H, Dost B. Seismic hazard due to small shallow induced earthquakes. vol. WR 2004-01. 2004.
[62] Eck van T, Goutbeek F, Haak H, Dost B. Seismic hazard due to small-magnitude, shallow-source, induced earthquakes in The Netherlands. Eng Geol 2006;87:105–21.
[63] Dost B, Goutbeek F, Eck van T, Kraaijpoel D. Monitoring induced seismicity in the North of the Netherlands: status report 2010. vol. WR 2012-03. 2012.
[64] NAM. Winningsplan Groningen. 2013.
[65] Orozova IM, Suhadolc P. A deterministic-probabilistic approach for seismic hazard assessment. Tectonophysics 1999;312:191–202.
[66] Mulders FMM. Modelling of stress development and fault slip in and around a producing gas reservoir. vol. PhD. Delft University of Technology; 2003.
[67] Bisch P, Carvalho E, Degee H, Fajfar P, Fardis M, Franchin P, et al. Eurocode 8: Seismic Design of Buildings Worked examples. Luxembourg: Publications Office of the European Union; 2012.
[68] Campbell KW, Bozorgnia Y. Updated near-source ground-motion (attenuation) relations for the horizontal and vertical components of peak ground acceleration and acceleration response spectra. Bull Seismol Soc Am 2003;93:314–31.
[69] Dost B, Eck van T, Haak H. Scaling of peak ground acceleration and peak ground velocity recorded in the Netherlands. Boll Di Geofis Teor Ed Appl 2004;45:153–68.
[70] NAM. Winningsplan Anjum. 2011.
[71] NAM. Winningsplan Ameland Oost. 2011.
[72] NAM. Winningsplan Ameland. 2011.
[73] Akkar S, Sandikkaya M a., Bommer JJ. Empirical ground-motion models for point- and extended-source crustal earthquake scenarios in Europe and the Middle East. Bull Earthq Eng 2014;12:359–87.
[74] NAM. Gaswinning vanaf de locaties Moddergat, Lauwersoog en Vierhuizen-Resultaten uitvoering Meet- en regelcyclus 2007-2012. 2013.
[75] Brady P V., Walther J V. Kinetics of quartz dissolution at low temperatures. Chem Geol 1990;82:253–64.